USGS
science for a changing world

Prepared for the National Aeronautics and Space Administration

Geologic Map of the Ganiki Planitia Quadrangle (V–14), Venus

By Eric B. Grosfils, Sylvan M. Long, Elizabeth M. Venechuk, Debra M. Hurwitz, Joseph W. Richards, Brian Kastl, Dorothy E. Drury, and Johanna Hardin

Pamphlet to accompany
Scientific Investigations Map 3121

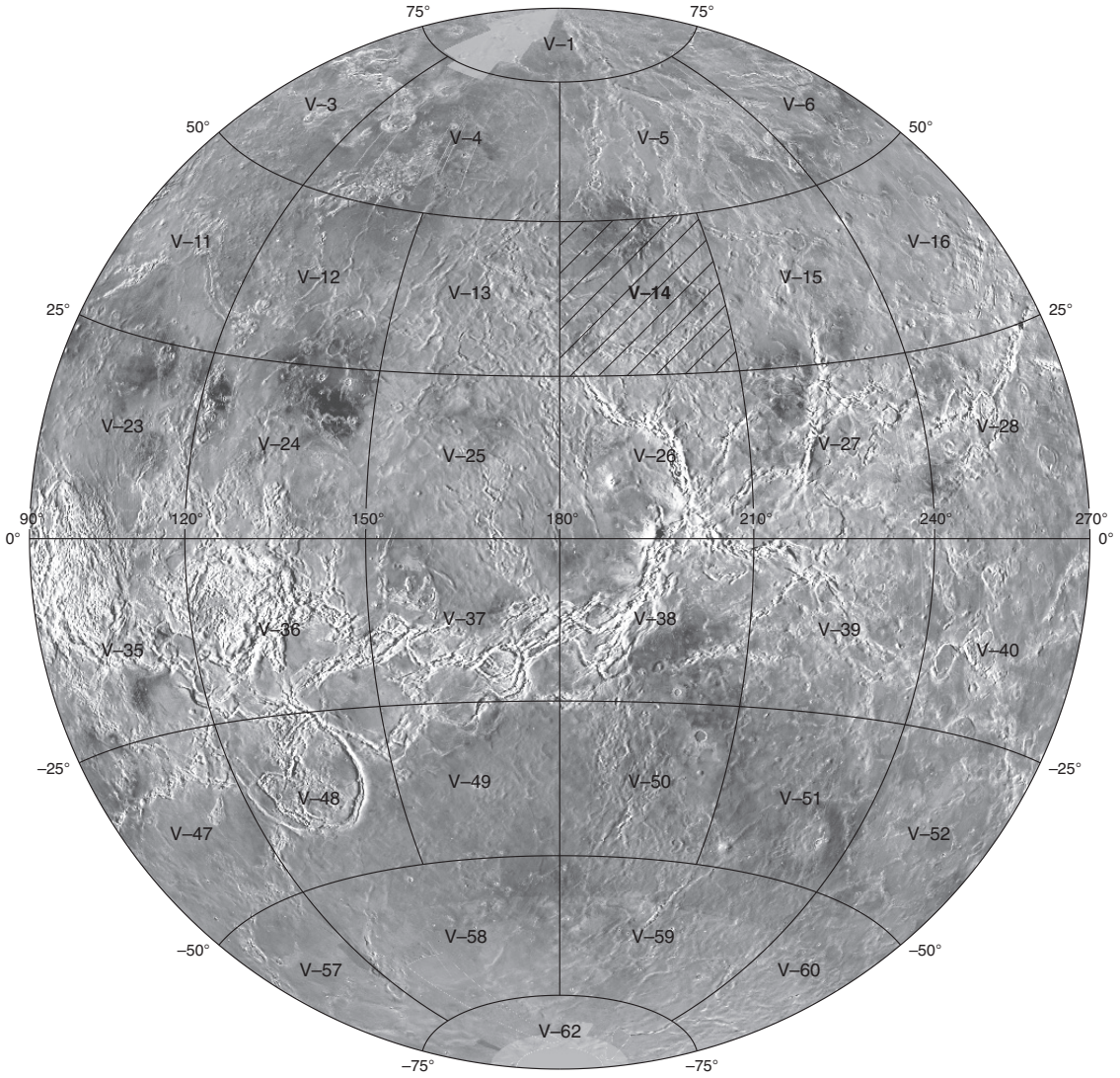

2011

U.S. Department of the Interior
U.S. Geological Survey

Contents

Tables

The Magellan Mission

The Magellan spacecraft orbited Venus from August 10, 1990, until it plunged into the Venusian atmosphere on October 12, 1994. Magellan Mission objectives included (1) improving the knowledge of the geological processes, surface properties, and geologic history of Venus by analysis of surface radar characteristics, topography, and morphology and (2) improving the knowledge of the geophysics of Venus by analysis of Venusian gravity.

The Magellan spacecraft carried a 12.6-cm radar system to map the surface of Venus. The transmitter and receiver systems were used to collect three data sets: (1) synthetic aperture radar (SAR) images of the surface, (2) passive microwave thermal emission observations, and (3) measurements of the backscattered power at small angles of incidence, which were processed to yield altimetric data. Radar imaging and altimetric and radiometric mapping of the Venusian surface were accomplished in mission cycles 1, 2, and 3 from September 1990 until September 1992. Ninety-eight percent of the surface was mapped with radar resolution on the order of 120 m. The SAR observations were projected to a 75-m nominal horizontal resolution, and these full-resolution data compose the image base used in geologic mapping. The primary polarization mode was horizontal-transmit, horizontal-receive (HH), but additional data for selected areas were collected for the vertical polarization sense. Incidence angles varied between about 20° and 45°.

High-resolution Doppler tracking of the spacecraft took place from September 1992 through October 1994 (mission cycles 4, 5, 6). Approximately 950 orbits of high-resolution gravity observations were obtained between September 1992 and May 1993 while Magellan was in an elliptical orbit with a periapsis near 175 km and an apoapsis near 8,000 km. An additional 1,500 orbits were obtained following orbit-circularization in mid-1993. These data exist as a 75° by 75° harmonic field.

Magellan Radar Data

Radar backscatter power is determined by the morphology of the surface at a broad range of scales and by the intrinsic reflectivity, or dielectric constant, of the material. Topography at scales of several meters and larger can produce quasi-specular echoes, with the strength of the return greatest when the local surface is perpendicular to the incident beam. This type of scattering is most important at small angles of incidence, because natural surfaces generally have few large tilted faces at high angles. The exception is in areas of steep slopes, such as ridges or rift zones, where favorably tilted terrain can produce very bright signatures in the radar image. For most other areas, diffuse echoes from roughness at scales comparable to the radar wavelength are responsible for variations in the SAR return. In either case, the echo strength is also modulated by the reflectivity of the surface material. The density of the upper few wavelengths of the surface can have a significant effect. Low density layers, such as crater ejecta or volcanic ash, can absorb the incident energy and produce lower observed echo. On Venus, a rapid increase in reflectivity exists at a certain critical elevation, above which high dielectric minerals or coatings are thermodynamically stable. This effect leads to very bright SAR echoes from virtually all areas above that critical elevation.

The measurements of passive thermal emission from Venus, though of much lower spatial resolution than the SAR data, are more sensitive to changes in the dielectric constant of the surface than to roughness. As such, they can be used to discriminate between roughness and reflectivity effects. Observations of the near-nadir backscatter power, collected using a separate smaller antenna on the spacecraft, were modeled using the Hagfors expressions for echoes from gently undulating surfaces to yield estimates of planetary radius, Fresnel reflectivity, and root-mean-square (RMS) slope. The topography data produced by this technique have horizontal footprint sizes of about 10 km near periapsis and a vertical resolution of approximately 100 m. The Fresnel reflectivity data provide a comparison to the emissivity maps, and rms slope parameter is an indicator of the surface tilts, which contribute to the quasi-specular component.

Ganiki Planitia Quadrangle

Introduction

The Ganiki Planitia (V–14) quadrangle on Venus, which extends from 25° N. to 50° N. and from 180° E. to 210° E., derives its name from the extensive suite of plains that dominates the geology of the northern part of the region. With a surface area of nearly 6.5 x 10^6 km^2 (roughly two-thirds that of the United States), the quadrangle is located northwest of the Beta-Atla-Themis volcanic zone and southeast of the Atalanta Planitia lowlands, areas proposed to be the result of large scale mantle upwelling and downwelling, respectively (see Bindschadler and others, 1992; Crumpler and others, 1993; Phillips and Hansen, 1998). The region immediately south of Ganiki Planitia is dominated by Atla Regio, a major volcanic rise beneath which localized upwelling appears to be ongoing (Bindschadler and others, 1992; Smrekar, 1994), whereas the area just to the north is dominated by the orderly system of north-trending deformation belts that characterize Vinmara Planitia (Zuber, 1987; Frank and Head, 1990). The Ganiki Planitia quadrangle thus lies at the intersection between several physiographic regions where extensive mantle flow-induced tectonic and volcanic processes are thought to have occurred.

The geology of the V–14 quadrangle is characterized by a complex array of volcanic, tectonic, and impact-derived features. There are eleven impact craters with diameters from 4 to 64 km, as well as four diffuse "splotch" features interpreted to be the product of near-surface bolide explosions (see Ivanov and others, 1992; Schultz, 1992). Tectonic activity has produced heavily deformed tesserae, belts of complex deformation and rifts as well as a distributed system of fractures and wrinkle ridges. Volcanic activity has produced extensive regional plains deposits, and in the northwest corner of the quadrangle these plains host the initial (or terminal) 700 km of the Baltis Vallis canali, an enigmatic volcanic feature with a net length of ~7,000 km that is the longest channel on Venus (see Baker and others,

1992; Bray and others, 2007). Major volcanic centers in V–14 include eight large volcanoes and eight coronae; all but one of these sixteen features was noted during a previous global survey (Crumpler and Aubele, 2000). The V–14 quadrangle contains an abundance of minor volcanic features including individual shield volcanoes and localized fissure eruptions as well as many small annular structures and domes, which often serve as the source for local lava flows.

The topographic and geophysical characteristics of the Ganiki Planitia quadrangle are less complex than the surface geology, but they yield equally valuable information about the region's formation and evolution. Referenced to the mean planetary radius of 6051.84 km (Ford and Pettengill, 1992), the average elevation in the quadrangle is –0.26±0.86 km (2σ) with a full range of –2.58 km to 1.85 km. The highest 2.5 percent of elevations in the quadrangle (above 0.60 km) are associated primarily with the major tessera blocks and the peaks of a few volcanic edifices, whereas the lowest 2.5 percent (below –1.12 km) mostly occur within corona interiors and in the northwest corner of the quadrangle where the plains begin to merge into the Atalanta Planitia lowlands. At the ~4.6 km/pixel scale of the topography data, the mean point-to-point topographic slope is 0.63° and topographic slopes greater than 2° cover less than 5 percent of the region. Overall, the topography of the Ganiki Planitia quadrangle can be characterized as flat, low lying, and nearly devoid of abrupt topographic variation. Complementing this gentle topography, the geoid anomaly has a generally linear gradient that decreases north-northwest from a high of ~20 m at the southern edge of the quadrangle (the northern border of the Atla Regio anomaly) to a low of –30 to –40 m along the northern edge (Konopliv and others, 1999). The vertical component of the gravity anomaly varies from ~50 mGal to –40 mGal (Konopliv and Sjogren, 1994), and integrated analysis of the gravity and topography data indicates that dynamically supported regions and areas of thickened crust are both present within the quadrangle (McKenzie, 1994).

Because the Ganiki Planitia quadrangle is a plains-dominated lowland area that lies between several major physiographic provinces (namely, Atla Regio, Atalanta Planitia, and Vinmara Planitia), a geologic map of the region may yield insight into a wide array of important problems in Venusian geology. The current mapping effort and analysis complements previous efforts to characterize aspects of the region's geology, for example stratigraphy near parabolic halo crater sites (Basilevsky and Head, 1995, 2002), volcanic plains emplacement (Basilevsky and Head, 1996), wrinkle ridges (Bilotti and Suppe, 1999), volcanic feature distribution (Crumpler and Aubele, 2000), volcano deformation (Lopez and others, 2008), coronae characteristics (Smrekar and others, 2003; Smrekar and Stofan, 2003), lithospheric flexure (Barnett and others, 2002), and various features along a 30±7.58° N. geotraverse (compare Ivanov and Head, 1999; 2001; 2004). Our current research focuses on addressing four specific questions. Has the dominant style of volcanic expression within the quadrangle varied in a systematic fashion over time? Does the tectonic deformation within the quadrangle record significant regional patterns that vary spatially or temporally, and if so what are the scales, orientations and sources of the stress fields driving this deformation? If mantle upwelling and downwelling have played a significant role in the formation of Atla Regio and Atalanta Planitia as has been proposed, does the geology of Ganiki Planitia record evidence of northwest-directed lateral mantle flow connecting the two sites? Finally, can integration of the tectonic and volcanic histories preserved within the quadrangle help constrain competing resurfacing models for Venus (see Basilevsky and Head, 1998; Nimmo and McKenzie, 1998; Phillips and Hansen, 1998; Guest and Stofan, 1999; Hansen, 2000)?

Mapping Techniques

The construction and analysis of the 1:5M scale map of the Ganiki Planitia quadrangle on Venus was performed using ArcView GIS software by ESRI, beginning with ArcView 3.1 and ending in ArcView 9.2. Magellan Cycle 1 synthetic aperture radar (SAR) images, with incidence angles ranging from 33.0–43.5° (Campbell, 1995), were used as the mapping base. Initial definition of map units was performed using full resolution 75 m/pixel FMAP images, mapped onto a Venus datum in sinusoidal projection, and standard mapping techniques (see Wilhelms, 1990) adjusted as necessary to accommodate both the interpretive challenges created when radar interacts with a planetary surface as well as the goals and scale of the mapping project (see Ford and others, 1989, 1993; Tanaka, 1994; Hansen, 2000). Material units were defined principally on the basis of their relative radar backscatter properties plus superposition and crosscutting relationships, and synthetic stereo images (Kirk and others, 1992) with 10x vertical exaggeration proved particularly useful for resolving the interplay between plains units and topography and hence for contact characterization. Contacts are defined as either certain or uncertain. A contact labeled "certain" is normally characterized by a sharp transition between adjacent units, sometimes topographically controlled. This label is used conservatively, and is intended to denote a unit boundary we identify and locate with a high degree of confidence. In some instances, the robustness of a "certain" contact was tested by having multiple authors map the same area to assess whether different mappers would place the contact in the same location. A contact labeled "uncertain" is one that shows a high degree of variability in placement between mappers, one that connects two "certain" contacts across an area where the contact is less well defined, or one which is gradational or approximate in location. As an example of the latter, where thin deposits of pr_2 onlap onto older pr_1 materials in an area with very little topography, the demarcation between the two is ill defined and so constrained to a zone rather than a specific linear contact, and thus the boundary between the two is only placed in a general way. Once defined, the material units and contacts were digitally transferred to a 250 m/pixel SAR base map image, prepared by the U.S. Geological Survey (USGS) in Lambert Conformal Conic projection, and the robustness of the defined units was evaluated using additional georeferenced Magellan datasets obtained from the USGS, including altimetry, emissivity, reflectivity and RMS-slope data. Secondary datasets, such as point-to-point slope maps at the ~4.6 km/pixel resolution of the altimetry datasets, were also constructed for use

during subsequent geological analysis. Major structural features were mapped at 250 m/pixel resolution, but interpretation of these features and the nature of their crosscutting and superposition relationships was enhanced through digital transfer onto the higher resolution sinusoidal imagery; such transfers within ArcView, including on-the-fly re-projection, can be accomplished through simple cut-and-paste operations, making integrated use of high resolution SAR imagery for interpretation and lower resolution data for the regional synthesis of information very straightforward. For clarity, not all mapped structural features are shown in the final map; instead, they are depicted in a representative fashion, largely limited to mapped structures greater than 30 km in length.

Two specific problems occurred during the mapping of the quadrangle. First, in some areas the structural deformation is so pervasive that it obscures the nature of the material unit being deformed as well as the presence of any pre-deformation material unit contacts; we define these regions as terrains. Second, several of the impact craters in the region are affiliated with extensive, radar-dark deposits that make it difficult to interpret the underlying material properties, contacts, and structures. This is particularly problematic for the radar-dark materials associated with the crater Yablochkina, which make the mapping process challenging across at least 0.88×10^6 km^2 in the northern part of the quadrangle. Taken together, such crater-derived, radar-dark deposits cover ~1.2×10^6 km^2 (~20 percent) of the mapped area.

Unit Physical Properties

Georeferencing and co-registration of different datasets within ArcView provides the opportunity to perform a more quantitative analysis of material unit properties than is possible within software products like Adobe Illustrator that are often used in planetary mapping. For instance, it is straightforward to calculate structural feature lengths and orientations, or to use map units as the basis for querying raster datasets, such as topography. This advantage is multiplied, however, because the form and transferability of the data allows future researchers who wish to conduct their own analyses using the mapped units to do so readily.

In past mapping studies, the remote-sensing properties of mapped units—backscatter, RMS slope, reflectivity, and emissivity—have normally been assessed using small "type" sample areas for a given unit. This approach is almost mandated for the incident angle-dependent backscatter because the data in the images must be corrected for their latitudinal position on a pixel-by-pixel basis before the backscatter from a given location or unit can be compared with another in a meaningful fashion. Most workers assess unit backscatter properties using software that adjusts a small selection of SAR image data for incidence angle and Muhleman calibration effects before ultimately yielding statistics for the selection in decibels (Campbell, 1995). This approach has the advantage that mappers can select areas they judge as representative and that lack structural deformation or other non-material artifacts that can locally alter the backscatter properties of the unit. However, there is some risk that the properties for the unit as a whole may not be well represented by the area(s) that are subjectively chosen, that non-material artifacts unrecognized by the mapper due to scale or other issues can still affect the backscatter, that little insight is gained into the degree of backscatter variability across the unit, and that the statistical error for the calculations is amplified by the small number of pixels typically sampled.

For our mapping and quantitative analysis of units within the V–14 quadrangle, we used ArcView to develop a simple (though computationally intensive) method for performing the same correction as Campbell (1995), thereby permitting location-specific, pixel-by-pixel conversion of backscatter to decibels across the entire quadrangle (Long and Grosfils, 2005). This approach has several advantages. First, by providing a chance to examine the entire material unit following conversion, we enhance the odds of identifying areas for sampling and analysis that are truly representative of the unit as a whole. This is particularly important when assessing the material characteristics of regional plains or other units that occur across a range of latitudes. Second, it may at times be advisable to eliminate the subjectivity involved with local sampling and instead simply calculate the material properties for a unit as a whole. Certainly this approach has the advantage that the large number of pixels sampled will enhance the robustness of the sampling. Third, it can provide a valuable, semi-quantitative opportunity to assess the degree to which, say, structural deformation has affected a unit. For example, an extensive regional plains unit with many obvious radar-bright structural features deforming it and a similar unit without much deformation will yield nearly identical mean backscatter values, but the standard deviation should be greater for the unit that has undergone deformation. Fourth, if bulk-material characteristics for a unit are desired without the contribution from non-material factors such as structural deformation, mapped structural features can be used (by buffering them in ArcView) as a basis for excluding deformed regions from the assessment of material properties; note that we did not take this step for our analysis here because it would have required far more detailed structural mapping than is suitable for a 1:5 million scale product. Performing a quadrangle-wide conversion of backscatter data can thus yield useful opportunities to complement and improve upon previous strategies for quantifying and comparing material unit properties. Material properties for the units and unit types in the Ganiki Planitia quadrangle are reported in tables 1 and 2, and backscatter variations are depicted in figures 1*A* and 1*B*.

Unit Robustness

A geologic map is meant to convey the mapmaker's interpretation of the region depicted. If three people map the same area and then compare their results, it is likely that some percentage of their boundaries and unit definitions will be very closely matched, whereas other areas will bear little resemblance from one map to the next (see Waldron and others, 2003). How, then, can one develop a sense of confidence that the material units being defined have robust qualitative and quantitative meaning?

Qualitative Evaluation

One approach, described in the previous section, is to use material unit properties to test whether units indeed appear to be different from one another, namely that the backscatter of materials mapped as a "radar-dark" plains units look more like one another than like materials mapped as "radar-bright" plains units. Whether subareas or entire units are sampled, however, the pixilated appearance inherent to radar backscatter data, and the natural variability in local surface properties within any given unit, often yield mean values that are indistinguishable from one another at a one standard deviation confidence level.

Another approach that can be used to gain confidence in a map product is to compare geologic map products prepared independently by different workers for the same area. This is particularly important for a global mapping effort because significantly different maps of the same or adjacent areas should raise concerns about how consistently a region's geology can be interpreted. For the Ganiki Planitia quadrangle, four qualitative comparisons were conducted. In the first three, comparisons of the map unit boundaries at 180° E., shared with the V–13 quadrangle (Ivanov and Head, 2005), at 210° E., shared with the V–15 quadrangle (J. Zimbelman, oral commun., 2003), and at 50°N., shared with the V–5 quadrangle (Rosenberg and McGill, 2001), reveal a high degree of consistency, with mapped unit boundaries and unit types/interpretations agreeing at approximately the 90–95 percent level; a map product for 25° N. (V–26) was not available at the time the current document was prepared. The principal differences identified stem from how a unit is or is not subdivided. For instance, in the V–14 quadrangle the Athena Tesserae are mapped as a single material unit because at 1:5 million scale the small handful of minor volcanic eruption products present within the tesserae are not significant enough to map as separate units. In the adjacent V–13 quadrangle, however, these kinds of erupted materials in Athena Tesserae were more significant and, therefore, they were mapped as separate units. Small variations in the way that features are "lumped" or "split" are common, and in general these variations do not result in significant differences in interpretation. For the fourth qualitative comparison, units mapped as part of a global 30° N. geotraverse prepared by Ivanov and Head (2001) were compared to the current map of the V–14 quadrangle south of ~37.5° N. When the two sets of map units are compared, the map unit boundaries and types agree at approximately an 80 percent level. The primary differences observed stem from either the manner in which the presence of structural deformation is incorporated into map unit definitions or from the differences in how features such as volcanic centers are characterized. Although interpretive differences that may be important occur in a few locations (for example, where we map the presence of large volcanoes that are not represented in the Ivanov and Head (2001) map), the general sense and location of material units in the two maps tends to be in reasonable agreement.

Quantitative Evaluation

The data presented in tables 1 and 2 (backscatter columns), along with the strong level of consistency between the Ganiki Planitia quadrangle map units and those defined by other workers, indicates that the map units we have defined are defensible. It is desirable, however, to test this confidence in a more quantitative fashion. Using the current map units as a "truth set," and taking advantage of all physical property raster data at our disposal (namely, radar backscatter, elevation, slope, surface emissivity, and surface reflectivity), we employed a weighted model-based clustering (WMBC) method designed to identify units whose quantitative properties are aligned more closely with a unit type other than the one assigned during the mapping (Richards and others, 2010). Model-based clustering (Banfield and Raftery, 1993; Fraley and Raftery, 2002) uses the Expectation-Maximization (EM) (Dempster and others, 1977) algorithm to fit a mixture of multivariate normal distributions to a dataset by maximum likelihood. Model-based clustering via the EM algorithm has been shown to produce accurate and stable clusters in a variety of disciplines (Banfield and Raftery, 1993). We use it to demonstrate that the mapped units (which were mapped without using the quantitative information explicitly) are consistent with the final clustering output from a WMBC algorithm that uses quantitative data.

The quantitative data from the maps (namely, radar backscatter, elevation, slope, surface emissivity, and surface reflectivity) are available in pixels. Because (a) we are using this technique to validate the map, and (b) using pixel data in clustering algorithms can overwhelm the computing time, we use summary statistics from each individual unit (specifically, for each unit, the mean pixel value and the standard deviation of the pixel values) as variables in the WMBC. Because the units are of unequal size, we expect the larger units to have a higher degree of classification accuracy; that is, a unit with more pixels will have means and standard deviations that better approximate the true mean and standard deviation for a particular unit. A unit with relatively few pixels will be more difficult to map and will have data values that might not reflect the unit type as accurately as larger units of the same type. In the WMBC algorithm, the parameters for each type of unit (for example, the characteristics that define a volcanic region) are calculated based on the initial units identified as that type. Without weighting, small units and large units will contribute equally to the unit type parameters. To create a more stable model, we down-weighted small units and up-weighted large units so that the characteristics of any particular unit type were more resistant to deviations in small units. Our simulations show that weighted model-based clustering is superior to standard non-weighted model-based clustering for situations when units are of considerably different sizes.

The basic clustering algorithm starts with an initial partition of the data (the current "truth" map) and models the different unit types based on the quantitative characteristics. Then, units are freely reallocated to the unit type for which their likelihood is highest. The model of the unit type characteristics is then recomputed and units are again allowed to be reallocated. The process continues until all units are allocated to the unit type for which they have the highest likelihood.

The results from the statistical test demonstrate that most units remain classified the same way as specified by the original geologic map, meaning, for example, that all areas mapped as

pr_1 (see Description of Map Units on map sheet) quantitatively resemble one another rather than any of the other unit types mapped. On the basis of their statistical characteristics, fourteen units (7 percent of the total) with a net area of 0.47 x 10^6 km^2 (~7 percent of the total) were consistently identified as misclassified, and for each case we re-examined the unit to determine if it had been mapped incorrectly. In all but one instance (a small tessera outlier reclassified as an edifice-fed flow unit), misclassification resulted when a geologically important piece of information integrated into definition of the unit during the mapping process was not picked up by the statistical algorithms. For instance, five units created by extensive eruption of lava flows from a low but sizeable central edifice (fe) were reclassified as regional plains units because in each instance the presence of the edifice topography was not significant enough for the statistical algorithms to distinguish the features quantitatively from flows lacking such an edifice as a source. Similarly, plains characterized by overlapping systems of eruptions from small (1- to 20-km-diameter) shield volcanoes (ps) were in some instances reclassified as regional plains because the subtle morphology of the small shield volcanoes yields no quantitatively robust signature for the algorithm to recognize. While user insight is still required to examine any possible misclassifications, the strength of this statistical technique is that it uses available raster data to test the internal consistency of the map units.

Based on the suite of tests performed, we have a high degree of confidence in the material units we have defined using standard geological mapping techniques. The units are in good agreement with independently produced maps adjacent to and partially overlapping our map area, and each type of unit is statistically distinct from all the others when the full suite of quantitative data at our disposal is employed. It is important to recognize that other workers mapping the same quadrangle might produce a different map that is equally valid. We feel confident that the current map provides a scientifically sound, internally consistent basis for conducting a geologic interpretation of the quadrangle.

Map Units

Different conventions exist for discussing map units and presenting their stratigraphy. Here, closely following the approach of Brian and others (2005), we divide our unit descriptions into general categories (for example, plains materials) for clarity. Values listed for the elevation, backscatter, and other parameters are reported for the complete area covered by a unit, unless otherwise noted; detailed information is included in both table 1 (summary by unit type) and table 2 (information for each unit). A detailed summary of the map unit stratigraphy is provided below and in the Sequence of Map Units, and typical examples of all plains materials and those derived from volcanic edifices or coronae are depicted in figure 2.

Heavily Deformed Units

Roughly 0.39 x 10^6 km^2 (5.9 percent) of the Ganiki Planitia quadrangle is occupied by complexly deformed regions called tessera terrain (unit t), characterized as radar-bright (–12.31 dB) materials so heavily deformed by at least two intersecting lineament sets that the precursor material(s) can no longer be recognized. Globally, tesserae occupy about 8 percent of the surface of Venus (Ivanov and Head, 1996), and in Ganiki Planitia each of the 56 blocks of tessera mapped is older than all other non-tessera units with which it is in contact. With a mean elevation more than 400 m above that of the quadrangle as a whole, tessera blocks uniformly exist as kipukas embayed by surrounding material units. Full accounting of the tessera structures is not performed for this 1:5 million scale mapping effort, but in general each tessera block is characterized by complex, short-wavelength, ridge-and-trough style deformation that is often uniform in nature within structural microterrains that can be similar to or different than the deformation preserved in adjacent microterrains. This deformation does not extend into the surrounding materials, with the possible exception in some places of fractures cutting unit pl (see "Local Plains Unit" section). The short-wavelength deformation is commonly punctuated by longer sets of fractures, troughs, graben and ridges that can be characterized well on a 1:5 million scale map, and our analysis of the tessera structures is thus limited here to a brief discussion of these features.

Parts of three major tessera terrains occur within the Ganiki Planitia quadrangle. The first, Nemesis Tesserae, occupies roughly 59 x 10^3 km^2 in the northwest quadrant, principally as three major blocks 50- to 100-km wide by 200- to 300-km long that together define a concave-north, east-west trending arc 1,400 km in length. The major structural lineaments across all three blocks have common characteristics, with one set comprised of extensional and contractional lineaments aligned roughly north-northeast and a second set comprised purely of extensional lineaments aligned roughly parallel to the local strike of the arc. The second major tessera terrain, Athena Tesserae, occupies roughly 63 x 10^3 km^2 in the southwest quadrant, principally as one major equant block a few hundred kilometers across with 10 smaller outliers tentatively assigned the name Athena as well on the basis of their proximity to the main block. Unlike Nemesis Tesserae, however, the major structural lineaments do not show a common pattern from block to block. This absence challenges assignment of the outlying blocks as Athena Tesserae material, or it could indicate that deformation within Athena was diverse at a shorter spatial scale. The deformation within the largest block of Athena Tesserae is remarkably uniform, however, with one set of contractional lineaments trending northeast and a set of extensional lineaments trending west-northwest. The third major tessera terrain, Lahevhev Tesserae, occupies approximately 242 x 10^3 km^2 in the south-central part of the quadrangle, principally as two main equant clusters of tesserae approximately 250 km by 500 km in size. The first of these blocks, located ~500 km east of the main block of Athena Tesserae, preserves structural trends of the same orientation, although the majority of lineaments in both sets are extensional. It appears possible that this block is being destroyed by the processes creating plains units pLh and pLl (see "Local Plains Unit" section). The second block, a few hundred kilometers southeast, shows the same west-northwest and northeast-trending extensional lineaments but is also cut by

a third dominant set of contractional structures with a northwest strike. Unlike the other tessera terrains, Lahevhev Tesserae has a strong positive residual topography signature indicative of a region of anomalously thick crust (McKenzie, 1994), which may help explain why Lahevhev preserves four times more material than the other major tessera terrains in the quadrangle.

While the blocks assigned to the three major terrains define the bulk of the tesserae in the quadrangle, twelve small tessera outliers ranging from a few hundred to a little over ten thousand square kilometers in size are sprinkled across the southeast, northeast, and northwest parts of the quadrangle. These outliers are too widely distributed and lack any common structural patterns to infer much about their origins. They are presumed to be remnants of larger tessera blocks that have been nearly obliterated by younger geological activity in the quadrangle, but the extent of these blocks is unconstrained by available data.

Deformation belt materials (unit bl) are highly elongate, heavily deformed regions which occupy 0.06 x 10^6 km^2 (0.8 percent), largely in the north-central and northeast parts of the Ganiki Planitia quadrangle. Like tessera, these units are characterized by a high degree of structural deformation, with both contractional (usually the earliest phases) and extensional deformation aligned along or slightly oblique to the gross trend of the belt as a whole. Locally, each is the oldest stratigraphic feature that has been preserved; in no area of the quadrangle are tessera terrain and deformation belt materials in direct stratigraphic contact, and the relative timing of these two units is unconstrained. Unlike tesserae, the deformation within unit bl has not been sufficient to obliterate the precursor plains, but the materials deformed by the ridges and fractures within the belt are preserved as broad kipukas distinctly different from their surroundings; therefore, these kipukas warrant definition as a local map unit and, in combination with the density and nature of the deformation, as a distinct geomorphic map unit label. In other locations throughout the quadrangle, for example Akawa Dorsa and Fornax Rupes, belts of intense structural modification are not classified as unit bl because the precursor and surrounding plains materials are clearly a single unit.

Local Plains Units

The Ganiki Planitia quadrangle contains nine plains units defined on the basis of their relative radar and morphologic properties. Six of these units occur in local areas: lineated plains material (unit pl), hummocky Lahevhev plains material (unit pLh), lineated Lahevhev plains material (unit pLl), Ganis Chasma plains material (unit pG), shield plains (unit ps), and homogeneous plains (unit ph). The remaining three units form more extensive regional-scale deposits (units pr_1, pr_2, and pr_3). All nine units have been deformed. In some instances the deformation crosscuts and is embayed by a given unit, which indicates emplacement and deformation of the material were occurring during the same time interval. In other cases, emplacement of a material unit appears to have been completed prior to the superposition of structural event(s).

Lineated plains material (unit pl; for an example see 37.6° N., 184.0° E.) occupies a net area of 0.33 x 10^6 km^2 (5.1 percent of the quadrangle area) and the twenty small locations mapped range in size from ~400 square kilometers to 143 x 10^3 km^2. In some locations, most occurring in the south half of the quadrangle, the unit is characterized by smooth, generally featureless material cut by a dense concentration of narrow extensional lineaments typically showing a uniform strike, although the lineament orientations are not constant from location to location. The majority of the mapped pl unit area, however, occurs within a discontinuous system of less deformed areas elevated above the surrounding regional plains and running east to west across the central part of the quadrangle. The majority of the deformation within these larger areas consists of east-west extensional structures (predominantly fractures) that trend roughly orthogonal to a much smaller number of contractional structures. Many small (<10 km in diameter) shield volcanoes are superimposed upon unit pl in these areas. In addition, unit pl defines the rims and near-rim areas of several coronae in the southeast corner of the quadrangle. All mapped locations exist as topographically elevated kipukas within younger surrounding terrains, and the average elevation of the unit is ~110 m above the mean for the quadrangle. The unit's mean radar backscatter (–14.28 dB, compared to a quadrangle mean of –15.79 dB) reflects the nature of the unit as an intimate mixture of intermediate backscatter material and radar-bright lineaments. Interpreted as volcanic plains later deformed by both extensional and contractional structures, unit pl is older than every other plains unit with which it is in contact (units pr_3, pr_1, pr_2, ps, and fe) and younger than the tessera terrain and deformation belt materials it abuts.

Ganis Chasma materials (unit pG) spatially associated with a major feature in the quadrangle, Ganis Chasma, occupy 0.16 x 10^6 km^2 (2.4 percent of the quadrangle) at a single location in the southwest corner of the quadrangle. Heavily deformed by the structures of the Ganis Chasma rift that cuts northwestward from Atla Regio, and aligned parallel to the rift's trend, unit pG has the strongest mean radar backscatter (–12.08 dB) of any material unit in the quadrangle. The source of the plains material is unconstrained—it does not visibly originate at either volcanic centers or rift structures within the quadrangle. The plains largely predate the structural deformation generated during the rifting event, but local small shield eruptions and a minor patch of unit pr_2 (at 26.0° N., 186.0° E.) embay several rift lineaments; this embayment indicates that minor eruptions continued within the area after the majority of the rifting was completed. With a mean elevation more than 620 m above that of the quadrangle, unit pG also lies at the highest mean altitude of all the unit materials mapped. Lower elevation areas to the north and south are covered by regional plains units. Unit pr_2 to the north embays unit pG and largely appears to cover the structures of Ganis Chasma, whereas unit pr_1 to the south embays unit pG but both covers and is crosscut by Ganis Chasma lineaments. Unit pG, interpreted as a volcanic plains unit that predates the Ganis Chasma rifting event, is preserved at elevation by uplift that occurred during the rifting process and is therefore older than all material units (units pr_1 and pr_2) with which it is in contact.

Lahevhev hummocky plains material (unit pLh) occurs in a single location, cutting east to west across the center of a large block of Lahevhev Tesserae. Centered at 28.3° N., 187.5° E. and covering an area of 12.5 x 10^3 km^2 (~0.2 percent of the quad-

range), unit pLh is characterized by gentle undulatory topography that forms an interconnected system of elongate peaks and troughs with a wavelength of ~10 km. In local areas, patches of smooth, undeformed plains occupy the troughs, and these materials have a radar signature indistinguishable from the material that forms the undulatory topography. The elongation direction of the peaks runs parallel to the boundary of the unit, and a dense network of radar-bright fractures with a similar strike has deformed the unit in most areas. The density of these radar-bright fractures appears to be largely responsible for the unit's high mean backscatter of –12.21 dB. While unit pLh shows almost 2 km of total relief, on average it lies some 500–700 m below the elevation of the surrounding tesserae, and the mean is ~50 m below the mean for the quadrangle. Parts of Lahevhev Tesserae to the north and south of unit pLh, as well as a block of tessera surrounded by unit pLh, show late-stage extensional deformation that strikes orthogonal to the alignment of unit pLh. The persistent presence of these orthogonal lineaments within the adjacent tesserae and their absence within unit pLh is indirect evidence that unit pLh is younger than the tesserae, an interpretation also supported by local embayment relationships. The origin of the materials and fabric defining unit pLh remains uncertain, but the nature of the topography, structural deformation, and stratigraphic relations suggests that unit pLh may be the end product of a complex sequence of geologic events. Namely, unit pLh may be the result of an intermingled sequence of extension (to form the unit-parallel fractures and down-dropped topography), volcanic eruption (to form the smooth plains materials in their deformed and undeformed states), and minor compression and/or shear (to generate the undulatory peak/trough topography) that has acted to rift apart and destroy a major block of Lahevhev Tesserae. Compared to the units with which it is in contact, superposition relations indicate that unit pLh is younger than the adjacent blocks of tessera (embays them, is not crosscut bv their structures), synchronous with unit pLl (no clear contact relations, and preserves the same structural deformation orientations and styles), and older than unit pr_2 (embays unit pLh).

Lahevhev lineated plains material (unit pLl; for an example see 27.0° N., 190.0° E.), like unit pLh, lies adjacent to and between large blocks of Lahevhev Tessera terrain. Spatially the unit forms four mapped blocks covering an area of 0.15 x 10^6 km^2 (~2.2 percent of the quadrangle), but two of these blocks have been subdivided into several pieces to call attention to key differences in their structural expression. Overall, unit pLl lacks the gently undulating surface characteristic of unit pLh, and like unit pl it shows expanses of smooth plains deformed by a pervasively distributed network of fractures; locally, these fractures are dense enough to obscure the nature of the material they deform. The fractures are commonly collected into narrow, slightly sinuous bands tens to hundreds of kilometers in length that are co-aligned with the dense lineaments seen in unit pLh, and both the structures and plains material are gradational across the inferred boundary between these two units; these characteristics cause us to interpret their formation as synchronous. Topographically, unit pLl lies at a mean elevation nearly 400 m above that of the quadrangle, and it defines a rough, deformed planum at an altitude exceeded only by the mean elevations of the tesserae and unit pG, the Ganis Chasma plains material. The strong radar backscatter (–12.41 dB) of unit pLl is similar only to the backscatters characteristic of the most tectonically modified materials in the quadrangle (namely, units t, pLh, and pG), and it therefore reflects the highly deformed nature of the unit. Interpreted as an elevated expanse of volcanic plains fractured by oblique extension, unit pLl is younger than adjacent blocks of tessera, is synchronous with unit pLh, and is older than units pr_1 and pr_2.

Shield plains material (unit ps; for an example, see 44.25° N., 197.5° E.), mapped at 17 locations scattered across the quadrangle, covers 0.55 x 10^6 km^2 (8.4 percent of the quadrangle). Unit ps has a high density of local surface flows erupted from vents at the apices of small, low-relief topographic cones interpreted as shield volcanoes (edifices less than 20 km across), which often gives the unit ps plains materials a mottled appearance. High densities of small shield volcanoes occur elsewhere in the quadrangle, but the defining characteristic of unit ps is that the flows from the numerous small shields and vents overlap sufficiently to be the predominant source of the plains material across an area exceeding 1,000 square kilometers. The mean elevation of the unit is within 50 m of the mean for the quadrangle, and thus the two mean elevations are indistinguishable given the vertical precision of the altimeter. Similarly, the mean radar backscatter for unit ps, –16.36 dB, is only slightly lower than the mean for the quadrangle as a whole (–15.79 dB). Stratigraphically, based on embayment and crosscutting relations, unit ps materials predate the deposits from unit ph and the unit fe materials from the only volcanic center to which they are adjacent (Dutrieu Patera), but they postdate all other material units with which they are in contact (units pr_3, pr_1, pr_2, pl, bl, co, and t); the timing of emplacement of cof materials from Nimba Corona is uncertain. These relations establish unit ps as one of the youngest in the quadrangle, a result at odds with findings which suggest that shield plains are a widespread unit that formed early in the stratigraphic sequence of many areas (see Basilevsky and Head, 2000; Ivanov and Head, 2004, and references therein). Some caution is warranted in any interpretation of this type of unit, however, because unit ps is defined by extensive sequences of small, overlapping volcanic deposits, and only the timing along the borders of the mapped material regions are well constrained. If a 20-km-diameter value is assumed to be typical for a small shield and its local deposits, then one can calculate to first order the area of unit ps, which contains small shields that do not lie in contact with other material units. Half of the small shield volcano deposits of unit ps in the Ganiki Planitia quadrangle are not in contact with other material units, and because the available stratigraphic information is not generally sufficient to unravel the internal chronology of small shield emplacement in detail within each mapped area of unit ps, the stratigraphy within the interiors of these units is poorly constrained at best.

Homogeneous plains material (unit ph) occurs in only one location (44.5° N., 193.5° E.) and covers an area of 0.01 x 10^6 km^2, or ~0.2 percent of the quadrangle. Lying at an elevation roughly 340 m above the quadrangle mean, the unit has a low radar backscatter (–19.45 dB) and is characterized by a rounded geometry, feathery margin, and lack of internal texture. Strati-

graphically, the unit is younger than units t, pr_2, and ps with which it is in contact, and interactions with older structures suggest that the unit varies in thickness. The basic geologic observations (feathery edges, mantling appearance, and association with young volcanic features) are not strongly consistent with lava flow emplacement, nor are the remote-sensing material properties (which indicate a very rough surface characterized by competent rock) consistent with an unconsolidated aeolian deposit (see Campbell and others, 1998). Taken together, however, the basic characteristics of the unit are such that we have interpreted unit ph as a possible pyroclastic flow deposit (Long and Grosfils, 2004). Although no source vent is evident, it is possible that the materials are locally derived, which implies the vent has been buried. It is also possible that the materials originated upon and flowed down the flanks of the large, unnamed volcanic rise (500 km in diameter and characterized by a fanning dike swarm, abundant small shield volcanism, and extensive sets of long lava flows plus unit ph) centered just east of the deposit. Because most models predict that a minimum of ~1.5–5.0 wt. percent CO_2 is necessary to create sufficient basaltic magma disruption for pyroclastic volcanism to occur on Venus (see Grosfils and others, 2000), it appears that the latest stage of local volcanic activity in the region was characterized by an unusually high concentration of volatiles.

Regional Plains Units

The Ganiki Planitia quadrangle has three major regional plains units: pr_1, pr_2, and pr_3. The oldest of the three, regional plains material 1 (unit pr_1), covers 0.86 x 10^6 km^2 (13.1 percent of the quadrangle; for an example, see 34.25° N., 195° E.) and is mapped at 14 locations, all of which occur in the south half of the quadrangle. The unit has a mean elevation ~180 m higher than the quadrangle as a whole, and the mean backscatter of –13.62 dB also indicates a somewhat rougher surface than the norm. Unit pr_1 has, relative to the other regional plains materials, a highly blotchy appearance. The plains are distinctive in this sense, displaying stratigraphically variable contact relations that are often ambiguous locally, but, when viewed collectively, indicate the unit has undergone a prolonged history of spatially and temporally patchy emplacement and modification. Based on the major lineaments mapped, the deformation preserved within unit pr_1 consists of twice as much extensional deformation as contractional by net lineament length, including the long array of complex fracturing that defines Fornax Rupes; extensional and contractional deformation are 1.7x and 1.4x more concentrated per unit area than the quadrangle mean (for details of this calculation, see "Structural Deformation" section). Where they are in contact, unit pr_1 material is younger than tesserae, lineated plains unit pl, unit pLl, and unit pG. They overlap in age with unit pr_2 in a few locations but are generally younger; they also interfinger stratigraphically with the structural deformation that defines Ganis Chasma. Unit pr_1 materials are older than unit ps and the lobate flow deposits from all named (Ninisinna Mons, Nimba Corona, Garland Patera, Kokyanwuti Mons (V–15), and the Waka Mons/Asintmah Corona complex) and unnamed volcanic centers (unit fe) they abut. Interpreted as an early formed suite of volcanic plains that has been preserved at many locations due to its higher-than-average elevation (for example, see 31.0° N., 182.0° E.), unit pr_1 provides a unique record of the complex volcanism and tectonism characterizing the early plains and history of the quadrangle.

The second era of regional plains emplacement is defined by regional plains material 2 (unit pr_2), a smooth, flat, generally featureless material that covers 2.66 x 10^6 km^2 (40.4 percent) of the V–14 quadrangle; for an example, see 40.5° N., 199° E. There are 25 mapped locations. One of these, occupying the west half of the quadrangle, accounts for 73 percent of the unit area. Three of the remaining 24, which lie within the central and northeastern parts of the quadrangle, define most (~22.7 percent) of the remainder. Unit pr_2 has a mean elevation ~110 m below that of the quadrangle (~300 m less than unit pr_1), and with a mean backscatter power of –17.84 dB it is one of the smoothest materials mapped. Emplacement of the unit appears to have occurred over a prolonged interval and, though unit pr_2 is younger than unit pr_1 in most locations, at a few the two are clearly contemporaneous. Unit pr_2 postdates tesserae, deformation belts, and the more heavily deformed plains (units pl, pLh, and pLl); is locally synchronous with but generally younger than unit pr_1; is locally synchronous with but generally older than unit fe; and predates all unit ph, ps, and pr_3 materials with which it is in contact. In the northwestern part of the quadrangle, unit pr_2 materials are cut by the Baltis Vallis channel. Structurally, unit pr_2 preserves approximately equal amounts of extensional and contractional deformation by net lineament length, and extensional and contractional deformation are 1.1x and 1.4x more concentrated per unit area than the quadrangle mean. Embayment relations with other material units and superposition of unit pr_2 locally on different lineament sets both indicate that unit pr_2 is a fairly thin deposit, and the unit is interpreted as smooth, low viscosity volcanic deposits that currently occupy many of the lower elevations of the quadrangle.

The final phase of widespread plains emplacement is characterized by regional plains material 3 (unit pr_3), which lies at a mean elevation 450 m below the average for the quadrangle (~350 m below unit pr_2). Unit pr_3 has a radar backscatter (–15.46 dB) almost indistinguishable from that of the quadrangle as a whole. Mapped at 12 locations, predominantly in the northeast quadrant of V–14, unit pr_3 covers 0.61 x 10^6 km^2 of the quadrangle (9.3 percent; for an example, see 44° N., 205.25° E.). Stratigraphically, unit pr_3 materials are older than unit ps and most volcanic centers (except Xtoh Mons) where these units are in contact. Unit pr_3 also postdates tesserae, deformation belts, and all other units with which it in contact (units pl, cof, and pr_2). Most (86 percent) of unit pr_3 occurs as a single continuous area with no evident source. Onlap relations reveal that this major unit pr_3 locale is thicker in the middle and thin at the edges. The other small patches of unit pr_3 generally have identifiable sources (a small volcano, for instance) but are similar in stratigraphic position. In the northwestern part of the quadrangle, a small deposit of unit pr_3 has flowed into and along the Baltis Vallis channel. Structurally, unit pr_3 preserves nearly four times as much contractional deformation as extensional by net lineament length, and extensional and contractional deformation are 0.43x and 2.3x more concentrated per unit area than the quadrangle mean. Unlike the older pr_1 and

pr_2 plains units, each location of unit pr_3 materials appears to define a stratigraphically brief, possibly single, emplacement event, and the unit is interpreted as young, somewhat rough, wrinkle-ridge-deformed volcanic plains deposits that currently occupy most of the lowest elevation areas in the quadrangle.

Edifice and Corona Units

In addition to volcanic plains, the Ganiki Planitia quadrangle contains an array of volcanic features including canali, major volcanic centers (of types mons, patera, tholus, corona, and unclassified; for definitions see http://planetarynames.wr.usgs.gov/index.html), and small volcanic edifices and domes. Some of these are responsible for the emplacement of material units preserved at the surface, whereas others are not. Here we describe the material units. Detailed descriptions of the discrete volcanic landforms are presented later, and stratigraphic placements are depicted on the Sequence of Map Units.

Volcanic edifice flow materials (unit fe), interpreted as volcanic lava flows originating at major edifices, cover 0.66 x 10^6 km^2 (10.0 percent of V–14; for an example, see 40° N., 206° E.). The average elevation of unit fe is within a few tens of meters of the mean for the quadrangle, and at –14.69 dB its average radar backscatter is slightly greater than that of the quadrangle as a whole. In general, the named and unnamed unit fe materials preserved at the surface are among the youngest in the quadrangle, and each named volcanic center is described herein. In cases where a specific example of material unit fe is constrained to originate at a named volcanic center, we have used arrows on the map to denote lava-flow directions away from the center.

Most coronae in the quadrangle are characterized by displacement and deformation of older surrounding plains, and they have failed to emplace distinct material units of their own. There are, however, some exceptions to this general rule. Corona rim materials (unit co) are older, uplifted plains materials, occupying 34 x 10^3 km^2 (~0.5 percent of V–14), and they are characterized by a backscatter (–15.69 dB) and mean topographic elevation similar to the quadrangle averages. These plains were mapped as a separate material unit when preserved in isolation upon elevated topography that has subsequently been embayed by younger material units. Structurally, unit co is deformed by a series of gentle, annulus-parallel contractional arches cut by contractional and extensional lineations. In addition, in two instances a corona has produced corona flow materials (unit cof), defined as smooth and generally featureless plains with a mean backscatter of –15.05 dB and a mean elevation ~200 m below the quadrangle mean. Based on observed geologic and geographic relationships, we interpret unit cof as lava flows derived from a nearby corona, and in total unit cof covers an additional 58.4 x 10^3 km^2 (~0.8 percent) of the quadrangle.

Impact Units

Impact crater formation within the quadrangle has produced two distinct material units. The first, present at every impact site, consists of crater material, undifferentiated (unit c). This material, covering 20.3 x 10^3 km^2 (~0.3 percent of the quadrangle), is characterized by a hummocky texture and irregular margins that together define the crater rim, interior walls and floor, and ejecta. As expected, the blocky nature of the surface materials yields a high mean backscatter (–13.24 dB), and on average the craters occur at a mean elevation (–340 m) that is quite low relative to the quadrangle mean. The largest crater in the quadrangle, Yablochkina, is also surrounded by a limited array of deposits mapped as crater flow material (unit cf), which has the lowest radar backscatter in the quadrangle (–20.52 dB mean). Characterized by a sheet-like geometry and arcuate, sharply defined margins, unit cf lies at a mean elevation of –130 m, and it appears be superimposed on the surrounding regional plains. The characteristics of unit cf are distinctly different than those of the dark halo deposits with which many of the impact craters are also associated; the dark-halo deposits are not a material unit, and we describe these deposits in detail herein when discussing the characteristics of each discrete impact crater.

Discrete Landforms Within V–14

Canali

Canali remain one of the most enigmatic volcanic features on Venus. As sinuous channels a few kilometers in width and many hundreds or thousands of kilometers long, it has been proposed that canali are produced when volcanic materials moving above or below a pre-existing plains surface generate a channel via thermal and/or mechanical erosion (see Baker and others, 1992; Gregg and Greeley, 1993; Lang and Hansen, 2006; Waltham and others, 2008). The northwest quadrant of the Ganiki Planitia quadrangle contains the initial (Baker and others, 1992) 700 km of Baltis Vallis, the longest channel of any kind (net length >7,000 km; Bray and others, 2007) thus far identified in the Solar System. The channel cuts materials of unit pr_2 and is partially filled in by younger unit pr_3 materials. It follows a northward course that is generally down gradient (regional slopes range from a few tenths to hundredths of a degree) but does not respond to gentle topographic undulations tens of kilometers wide, hundreds of kilometers long, and hundreds of meters tall. Similarly, the channel does not respond to the presence of local structural deformation, which is clearly younger where the two intersect. The channel width varies from 1.5 to 4.5 km, and it is mapped in four segments. Three of these segments form a braided system separated by breaks of at most a few kilometers, possibly caused by later structural or volcanic activity, whereas the fourth is separated from the others by ~100 km. The most direct path between the braided components and this fourth segment aligns with and is heavily deformed by a large wrinkle ridge—these relations indicate that all four segments might once have been connected. No source region for the channels is evident. The southernmost ends of the braided and fourth segments are 150 km north and 180 km east-northeast, respectively, from Nijole Mons, and it has been proposed previously (Baker and others, 1992) that this volcano may be the source region for Baltis Vallis. This proposed hypothesis

is not supported by our mapping efforts, because there is no evidence to suggest that either younger volcanic deposits or structural deformation has affected the area separating the edifice and channel ends. The fourth segment ends adjacent to the major, previously unrecognized volcanic rise associated with unit ph, however, and it is possible that this rise is linked to the origin of the canali as it is similar in stratigraphic position and is located fairly close by.

Major Volcanic Edifices

There are materials from ten named volcanic centers within the Ganiki Planitia quadrangle, including one tholus, four patera, and five mons. Individually they cover areas from 18 to 214 x 10^3 km^2, and each is described separately herein.

Apakura Tholus (40.3° N., 208.8° E., diameter 10 km) is a small, domical volcanic edifice that has erupted materials of unit fe that cover more than 64 x 10^3 km^2 (~1.0 percent of V–14). With a mean elevation 500 m below that of the quadrangle, the Apakura Tholus materials have a total relief of 1,100 m and a radar backscatter close to the mean for the quadrangle (–15.79 dB). Lobate and sheet flows define a broad, roughly circular stack of material extending 120 to 170 km from the central vent area, with a longer set of lobate flows extending nearly 400 km to the east. Apakura Tholus flows embay unit pr_3 to the north, east, and west and are, in turn, embayed by flows from Shala Mons to the south. The dominant north-south wrinkle ridges that cut unit pr_3 in this area both deflect and crosscut the Apakura Tholus flows, and these relations indicate that formation of this structural set and eruption of the Apakura Tholus lavas were contemporaneous events.

The Ganiki Planitia quadrangle contains four patera. Two of these, named prior to the current mapping effort, are not the source of any specific surface materials. Izumi Patera (50.0° N., 193.6° E.), which lies at the northern boundary of the quadrangle, is recognizable due to the presence of a 15- to 20-km-wide topographic annulus some 75 km in diameter, which rises 300 m above the depression it encloses and 300 to 400 m above the surrounding plains. In fact, Izumi somewhat resembles a small corona; however, it shows only minor contractional, circumferential deformation along the inner and outer edges of the annulus. The topographic deformation has uplifted the unit pr_2 materials exposed throughout the area and therefore Izumi postdates unit pr_2 at this location. Razia Patera (46.2° N., 197.8° E.) is also comprised of, and thus younger than, unit pr_2 materials, and like Izumi it has many characteristics in common with coronae. Peanut-shaped overall, the long axis of Razia Patera extends 150 km north-south and 50 km east-west. Topographically, the 20- to 35-km-wide rim of the patera rises 200 to 400 m above the enclosed depression, but it also has a distinct structural signature, with extensional lineaments aligned tangential to the rim while short contractional structures, confined to the elevated annulus topography, are aligned normal to the rim. Based on deflection of regional wrinkle-ridge sets into a pseudo-radial alignment as they approach Razia Patera, this volcanic feature was present prior to the contractional deformation that crosscuts unit pr_2. Unit pr_3 abuts against the annulus topography to the south and, while numerous small shields occupy the center of the patera, its floor is covered predominantly by unit ps materials that have flowed into the central depression via a breach located in the southwestern part of the annulus.

Dutrieu Patera (33.8° N., 198.5° E.), like Razia Patera, is peanut-shaped, and it extends 150 km north-northeast by 75 km west-northwest. Surrounded by a topographic annulus 200- to 500-m tall and 20- to 35-km wide, the interior of the patera lies 200 to 600 m below the level of the surrounding unit pr_2 and unit ps plains materials. The mean elevation of the Dutrieu Patera deposits is 120 m below the mean altitude of the quadrangle, and the relief of 1.3 km extends from 800 m below the mean to 500 m above it. The annulus and interior of the patera consist of lobate and sheet materials of unit fe with a mean backscatter of –14.66 dB; together these materials cover 30.4 x 10^3 km^2 (~0.5 percent of V–14). Initial eruptions from the patera thus predate formation of the annulus and central depression, and this finding suggests that a complex interplay between volcanic activity and topographic adjustments was required to form the final patera morphology. Based on crosscutting and embayment relations, the unit fe materials defining the bulk of the patera are embayed to the south and west by unit pr_2. These same unit pr_2 plains are themselves embayed by unit fe materials, erupted from the outside edge of northern Dutrieu Patera, which extend 150 to 175 km east and west from the inferred eruption site and partially wrap around the patera topography. To the west, the older unit fe flows of Dutrieu Patera are in contact with extensive unit ps plains materials; stratigraphic timing information along this contact is sparse but indicates interfingered emplacement of the two units, with most of unit fe predating most of unit ps. The younger flows from Dutrieu Patera, however, are clearly superimposed upon unit ps. Taken together, these data indicate that Dutrieu Patera was a long-lived volcanic center emplaced during an interval that encompasses the same period of time over which local unit pr_2 and unit ps materials were forming.

Garland Patera (32.7° N., 206.8° E.), the smallest of the four patera within the Ganiki Planitia quadrangle, is characterized by a mean elevation identical to that of the entire quadrangle and a 40- to 45-km-diameter annulus of fractures; a faint outer network of circumferential fractures extends at least another 40 km to the southeast, however, defining a broader, egg-shaped pattern of deformation. The main annulus, coinciding coarsely with a topographically elevated rim 10- to 15-km wide that rises 400 m above the mean elevation of the unit, surrounds a depressed area that extends 500 m below the surrounding plains; these relations create nearly a kilometer of local relief. Surrounding the annulus, rough lobate and sheet materials of unit fe with a mean backscatter of –12.57 dB extend 80–100 km to the northeast, southeast, and southwest, covering 18.4 x 10^3 km^2 (0.3 percent of V–14). Based on observed superposition and crosscutting relations, the Garland Patera unit fe materials are everywhere superimposed upon the surrounding pr_1 unit, and in most locations the structural features that deform unit pr_1 also terminate at the contact or a short distance into the fe unit. However, several northwest-trending wrinkle ridges, north-south-trending fractures, and the bulk of the fine-scale extended annular deformation crosscut

unit fe unit locally; these characteristics suggest that several minor episodes of deformation postdate the interval during which the bulk of unit fe was emplaced. Taken together, these data indicate that Garland Patera is a volcanic center that postdates the bulk of the adjacent regional plains emplacement and deformation, although there are clear indicators that externally driven regional deformation as well as late-stage endogenic deformation (perhaps the initial phases of a larger collapse) also occurred within the feature to a limited extent.

The Ganiki Planitia quadrangle contains five montes, only one of which (Nijole Mons, see Burba and others, 2001) had previously been named. The main Nijole Mons edifice (45° N., 185° E.), circular in plan view, has ~1,250 m of domical relief across a diameter of 60 km, and a small secondary dome 20–25 km across occupies its summit position. Owing to its spatial coincidence with Akawa Dorsa it is difficult to tell how much of the edifice is constructional and how much derives from the arched topography of the underlying Dorsa. The apron of unit fe materials surrounding Nijole Mons out to a distance of ~50 km beyond the main edifice is also unusual, characterized by a wispy appearance and a very low backscatter (–17.10 dB). The contact between these materials and the adjacent unit pr_2 lowland plains, also mottled and characterized by low radar backscatter, is poorly defined, and the apron is not marked by any other distinctive physical properties (for example, emissivity); at most the Nijole Mons materials cover 18 x 10^3 km^2 (~0.3 percent of V–14). We interpret the wispy materials as thin, sheet-like lava flow deposits, while noting that an explosive emplacement mechanism, although unlikely, cannot be ruled out. If the lava flow interpretation is correct, the apron of Nijole Mons flows is superimposed upon unit pr_2 yet is clearly crosscut by the wrinkle ridges within Akawa Dorsa and the surrounding plains; these relations indicate that much of the local structural deformation within the Dorsa postdates the formation of Nijole Mons.

In sharp contrast to Nijole Mons, Ninisinna Mons (25.7° N., 197.5°E) is surrounded by a complex sequence of lobate, high backscatter (–11.97 dB) unit fe materials that cover an area of 30.7 x 10^3 km^2 (~0.5 percent of V–14). The central, heavily deformed edifice is surrounded by an annulus of fractures some 100 km in diameter. The lobate unit fe materials originate both at and from within the interior of this circumferential feature, and the stratigraphy indicates that the annular deformation and emplacement of the lobate flow materials overlapped in time. The region within the annulus is elevated as much as 2.5 km above the area outside it, and the average elevation of the Mons and associated unit fe materials is 590 m above the mean for the quadrangle. The lobate apron of flows is superimposed upon or abuts against the surrounding unit pr_1 plains, adjacent parts of Lahevhev Tessera, a set of unit fe materials 100 km to the south (the source of these flows appears to be external to the quadrangle or obscured by gaps in the radar coverage), and upon a second set of unit fe plains 200 km to the north. The second set of fe plains are inferred to originate from a set of three or four small volcanic centers in that area, and the similarity between the characteristics of these smaller centers and Ninisinna Mons, particularly structurally and topographically, suggests that they may share a common volcanic heritage. Finally, the lobate apron and edifice are crosscut by younger structural lineaments that define the southernmost extent of Fornax Rupes within the quadrangle. We thus infer that Ninisinna Mons is the most recent feature constructed within a broader area characterized by a persistent, self-similar style of volcanic activity, and that this period of volcanism from local centers postdates regional plains emplacement but predates the tectonic activity responsible for creation of the younger Rupes.

Shala Mons (39.4° N., 208° E.) is a flat, minimally deformed volcanic edifice 90 km across that has erupted materials of unit fe covering more than 58 x 10^3 km^2 (~0.9 percent of V–14). With a mean elevation 460 m below that of V–14, the low-lying Shala Mons deposits have a total relief of 1,300 m and a radar backscatter (–15.01 dB) only slightly greater than that of the quadrangle as a whole. Lobate and sheet flows extend significant distances to the east (>175 km), south (~220 km), and west (~650 km), and there are subtle topographic indications that an arcuate or ovoid annulus 50–60 km across has been almost completely buried by the flows just south of the volcano's crest. The flows to the south and east are superimposed upon unit pr_3 and unit pr_2 materials as well as sheet-like unit fe deposits that appear to originate from Kokyanwuti Mons in the adjacent V–15 quadrangle. To the north, late-stage flows from Shala Mons are superimposed on Apakura Tholus; the flows' failure to extend more than 75–100 km in this direction is inferred to be a result of abutment against the pre-existing Apakura Tholus topography. Finally, the narrow, laterally extensive flow deposits to the west occupy the topographic low between Apakura Tholus and an unnamed sequence of small volcanic centers forming a linear ridge that extends northwest from Madalait Corona. The narrow Shala Mons flows crosscut or embay unit pr_3 and unit pr_2 materials, and they also abut a sequence of unit fe materials that are spatially correlated with the linear array of volcanic centers and are inferred to originate from them; however, the nature of the stratigraphic contacts between the two fe units leaves their relative timing uncertain.

Waka Mons (26.3° N., 207.7° E.) is perhaps the most distinctive and unusual edifice within the quadrangle. The main edifice, roughly 1,000 m high and 50–60 km in diameter, is superimposed upon the northern rim of Asintmah Corona. A complex system of lobate flows clearly emanates from Waka Mons, and it extends about 200 km in all directions. These lobate flows were preceded by sheet-like deposits that cover the surrounding plains across radial distances extending as much as 500 km. It is unclear whether these sheeted flows derive from Waka Mons or Asintmah Corona, and they have thus been mapped in combination with the lobate flow sequence as a single unit fe, which has a mean backscatter of –14.84 dB. This unit covers 213 x 10^3 km^2 (~3.2 percent of V–14), but it also extends significant distances into V–15, V–26, and V–27, and we estimate that the net area of the deposits could be twice that of the exposure within V–14. Within the V–14 quadrangle, this fe unit embays all others with which it is in contact (units fe, pl, pr_3, pr_1, and pr_2), and in many instances it follows paths clearly guided by pre-existing topography (for example, the remaining rim of Benzozia Corona and the small shield deposits within its interior). Like most of the edifices within the quadrangle, Waka Mons as well as the surrounding deposits

are only minimally deformed by tectonically generated features such as wrinkle ridges that affect the regional plains. Unlike most other edifices, however, Waka Mons is characterized by a distinctive set of fractures arrayed radial to the summit, features that are inferred to be the surface expression of subsurface dike emplacement. These fractures, which extend ~100 km from the summit region, both crosscut and are embayed by the lobate flow deposits; these characteristics indicate that their emplacement was coeval. A second set of radial fractures, centered upon an annular structure southwest of Asintmah Corona, also crosscuts and is buried by the Waka/Asintmah unit fe materials. In contrast, this set of radial lineaments, also interpreted as a dike swarm, extends more than 1,000 km northeast from the focal point. Taken together, these observations indicate that the extensive extrusive and intrusive activity within the Waka/Asintmah complex was interfingered in time, and crosscutting and superposition relations clearly demonstrate that the voluminous volcanism characterizing this region was one of the most recent events to affect the quadrangle.

Another major edifice within the quadrangle, Xtoh Mons (39.7° N., 194.2° E.), is also highly unusual. The main edifice sits at the intersection of three topographically elevated regions of deformation arrayed in a distinctive Y-shaped pattern, and sheeted materials from Xtoh Mons embay these materials (units bl and pl) and flow down-gradient into the adjacent lowland areas in three locations, where they cover unit pr_2 materials and are in turn embayed by unit pr_3 to the east. The main edifice rises roughly 1,000 m above the elevation of the surrounding deformation belts, but the mapped unit fe deposits, with a mean backscatter of –15.68 dB, are characterized by almost 2,500 m of relief across the entire area of the volcano, 44 x 10^3 km^2 (~0.7 percent of V–14). Like Waka Mons, Xtoh Mons lies at the focus of an extensive system of radiating lineaments inferred to be the surface expression of a system of dikes that propagated laterally away from the edifice. The lineaments crosscut units fe, bl, pl, and pr_2 units across distances of as much as 400 km, but they are generally absent from unit pr_3, although faint traces of the lineaments can be seen in a few places near the edge of unit pr_3. We thus infer that extrusive and intrusive activity at Xtoh Mons predates unit pr_3 and that thinner cover exists in those areas that lie at slightly higher elevations, where the partially covered lineaments can still be observed.

Smaller Volcanic Features

In addition to larger edifices, V–14 also contains several thousand small shield volcanoes less than 20 km in diameter that are sprinkled across the quadrangle. The quantity of small shields observed is far fewer than the numbers reported for many other plains-dominated regions (see Hansen, 2005); the average density of small shields in V–14 is only 0.5 shields per thousand square kilometers. The average elevation at which shields occur is 50 m above the mean elevation for the quadrangle as a whole, and 95 percent of the shields are distributed within ±730 m of this elevation. Individual shield locations, however, are not randomly distributed relative to the mapped material units, and they often define clusters that ignore material unit boundaries. Unsurprisingly there is a high number (~30 percent) and concentration (1.6 shields per thousand square kilometers) of small shields within unit ps, where shield-fed deposits create the material mapped; however, the major regional plains units, where 50 percent of the small shields can be found, also reveal significant spatial distribution variations. Unit pr_1 materials, generally older and preserved at higher elevations than the other regional plains units, have a concentration of small shield volcanoes that is the same as that of the quadrangle overall (namely, 0.5 shields per thousand square kilometers). These shields tend to be irregular in planform and are spread throughout the different occurrences of pr_1 that have been mapped. Unit pr_2, generally younger than unit pr_1 and older than unit pr_3, has a concentration of slightly less than 0.4 shields per thousand square kilometers. The majority of these small shields tend to be smaller, rounder, and they occur near the boundaries of pr_2, in close proximity to other higher elevation materials on which unit pr_2 onlaps; small shields are mostly absent from the interior parts of the pr_2 units. Clear exceptions to this pattern occur, for instance in the southwest corner of the quadrangle where a high concentration of shield volcanoes is observed on unit pr_2 materials, but in general most of these small shields are interpreted as kipukas that predate emplacement of the pr_2 units with which they are associated (see Ivanov and Head, 2004). Finally, the concentration of small shields in unit pr_3 is very low, less than 0.2 shields per thousand square kilometers, and essentially no small shields occur within the unit interior. The remaining ~20 percent of small shields within the quadrangle generally avoid tesserae and the younger unit fe materials, and they are instead concentrated almost entirely within the elevated lineated plains regions (unit pl) and upon elevated corona rims. Given the number of small shields and their geographic distribution, it appears possible that (1) concentrations in older units reflect a greater accumulation period for temporally random shield emplacement, (2) small shield emplacement occurred predominantly during the period predating regional plains emplacement, which suggest shields in the plains areas have been buried by the younger plains deposits, or (3) some process focuses melting and shield emplacement within higher elevation units, perhaps due to the presence of thicker crust, or because volcanism taking place at lower elevations occurs via different mechanisms (for example, plains-forming surface eruptions) than those which occur at higher elevations (for example, perhaps magma stalling and hence reservoir-derived volcanism predominates; Head and Wilson, 1992).

In addition to the limited number of large volcanoes and the significantly greater quantities of small shield volcanoes described above, there are thirty distinctive, small (diameters of less than 20 km) and intermediate (diameters of more than 20 but less than 100 km) sized edifices clustered in the north-central and southeastern parts of the quadrangle. Ranging from 7 to 23 km across, these edifices show an array of different topographic, structural, and volcanic characteristics. Over a third of the volcanoes (n=11) have a single large caldera, while another eight have one or more small pits near their summit. Caldera diameters range from 2 to 10 km with a mean between 5 and 6 km, and caldera-to-edifice diameter ratios range from 0.2 to 0.6, illustrating that the calderas generally define a significant

part of the edifices with which they are associated. Ten of the volcanoes (33 percent) are best classified as steep-sided domes, nine of the volcanoes (30 percent) have bulbous or convex-up topography (that is, domical), and eight (27 percent) have steep conical geometries. Of the remaining three volcanoes, one is shield-like, one is best characterized as a volcanic depression, and the third has an irregular geometry and may have undergone volcanic spreading (for further description of this volcanic spreading, see 47n198FD in Lopez and others, 2008). Twenty of the thirty edifices lie within regions mapped as unit pr_1 or unit pr_2 plains; one occurs within a tessera block, one within unit pl, one within unit pr_3, and the remaining six are associated with unit fe materials. Individual edifices both post- and pre-date the map units with which they are geographically associated; these relations suggest that their formation was at least in part synchronous with their surroundings, and no distinct stratigraphic patterns otherwise emerge for the set as a whole.

Coronae

We identify eight coronae—large, often morphologically complex volcano-tectonic features characteristically showing a near-circular annulus of structural deformation—within the quadrangle. Five of these (Asintmah, Benzozia, Madalait, Qakma, and Neyterkob (defined as a multiple corona structure, therefore including Cerridwen)) were identified previously by Stofan and others (2001) as Type 1 coronae, one (Embla) was defined as a Type 2 corona, and three (Benzozia, Cerridwen, and Neytercob) were defined as coronae by Crumpler and Aubele (2000). In addition, however, there are differences between these catalogs and the results of the current mapping effort. For instance, the catalog of Stofan and others (2001) lists four additional features, each classified as a Type 1 corona, that we do not map as coronae. Two of these (30.3° N., 209.7° E.; 28.8° N., 209.4° E.) appear to lack key structural (plus volcanic or topographic) characteristics of coronae, while for the other pair (29.4° N., 195.5° E.; 29.8° N., 191.6° E.) each feature is formed by deflections of regional structural trends around elongated low-lying areas; in all four instances we were not convinced that the observed characteristics require a corona-style formation mechanism, although this is certainly one possibility. Crumpler and Aubele (2000) classify Asintmah Corona as a large volcano instead of separating it from Waka Mons, and they also classify Embla, Madalait, Nimba and Qakma as arachnoids. Though widely used, the term "arachnoid" is not currently a formal classification recognized within the U.S. Geological Survey planetary nomenclature scheme, and the dominance of the radial patterns (present at only some of these coronae) does not in our view warrant their primary classification as an Astrum, a radial-patterned feature.

Asintmah Corona (25.9° N., 208° E.) is a gently elongated feature, roughly 170 km north-south by 115 km east-west, characterized by a poorly defined annulus of ridges and sub-parallel extensional lineaments. The lineaments generally radiate away from Waka Mons on the northern edge of the corona rim, whereas a faint set of circumferential lineaments is best seen on the southeast part of the corona rim; the southeast part of the corona is also where the rim is most readily observed. Heavily modified, the rim is 30–40 km across and, while elevated in some locations by as much as 200 m, is generally level with the corona interior and surrounding plains. Asintmah Corona does not appear to be the source area for any material units currently preserved at the surface.

Like Asintmah Corona, Benzozia Corona (27.5° N., 204.5° E.) and the Embla Coronae (28.9° N., 205.4° E.) are interpreted as relatively old, relict structures. Neither appears to be the source of specific material units, and the coronae interiors contain a concentration of small shield volcanoes. Benzozia Corona has a diameter of roughly 180 km. The western side of the corona is the best preserved, with a rim 30 km across rising approximately 500 m above the surrounding plains and corona interior. This elevated region exposes unit pl materials, with structures that adopt circumferential alignments, that were first embayed by unit pr_2 plains and then by unit fe materials originating at Waka Mons. The fe materials, which breach the corona rim on its southeast edge, clearly delineate the presence of an internal topographic moat and flow northwestward in two narrow circumferential bands as they hug the interior wall of the corona rim. The Embla Coronae are a pair of small annular structures, together 130 km across from northeast-southwest and 80 km from northwest-southeast, that also preserve unit pl materials on their elevated rims. These materials are embayed by unit pr_2 to the west and south, by unit fe materials from Waka Mons on the north, and by unit pr_3 materials on the east that also breach the southernmost corona rim and flood its low-lying interior.

Cerridwen Corona (49.6° N., 201.8° E.) and Neyterkob Corona (49.7° N., 204.7° E.), each in excess of 200 km across, share a rim and thus form a multiple corona system shaped like a squashed infinity symbol; the pair is bisected by the boundary with the Pandrosos Dorsa (V–5) quadrangle and hence is described as well by Rosenberg and McGill (2001). Unit co materials occur on the elevated rims of both coronae, and these materials are embayed by younger plains deposits. In addition, an elongated kipuka of corona flow materials (unit cof) covering 39.5×10^3 km^2 to the south of the coronae is interpreted as lava flows derived from Neyterkob. Both co and cof materials are embayed by unit pr_2 plains that fill in low-lying areas and, therefore, structural features preserved within unit cof are not generally visible for more than a few tens of kilometers into unit pr_2 or an adjacent patch of unit pr_3. The interior of Cerridwen, which lies roughly 1 km below the rim elevation and up to a few hundred meters above the surrounding plains, also contains numerous small shield volcanoes. The ps unit they create occupies the interior floor of the corona. The characteristics of the Neyterkob Corona interior are quite similar; unit ps materials lie roughly 1.2 km below the adjacent rim, and they occur at roughly the same elevation as the immediately adjacent plains to the south and east.

Madalait Corona (37.6° N., 206.4° E.), 160 km northwest-southeast by 120 km northeast-southwest, is part of a northwest-trending chain of structures of probable volcanic origin. The corona is characterized by an elevated rim (~800 m above the surrounding plains) and low-lying interior (~200 m below the surrounding plains). The interior has a high concentration of small shield volcanoes. Formation of the rim appears to

have displaced unit pr_2 materials, which indicates the corona formed after the local unit pr_2 deposits were emplaced. The rim is embayed by unit pr_3 and unit fe materials on three sides, and the overlapping deposits from the shield volcanoes in the corona's interior form unit ps materials that also postdate formation of the rim. Nimba Corona (32.8° N., 204.5° E.), 90 km in diameter with a structurally defined annulus of extensional fractures, deflects and thus postdates the regional unit pr_1 materials within which it is located. The interior of the corona is fairly flat, slopes gently down to the southeast, but is elevated up to a kilometer above the surrounding plains. Unit cof materials, also interpreted as lava flows associated with the corona, are superimposed as faint lobate deposits directed downslope on unit pr_1 and cover a net area of roughly 19 x 10^3 km^2; these same unit cof deposits are in contact with units ps and pr_2 but the stratigraphic relations with these units are less certain. A pattern of pseudo-radial ridges is observed within units cof and pr_1, visible most clearly on the north and west sides of the corona; these features are not observed to cross into units pr_2 or ps.

Qakma Corona (35.5° N., 207.1° E.), like Nimba Corona, is a small circular feature (120 km across) with an annulus characterized by circumferential extensional lineaments that serves as the locus for a system of radially aligned ridges. The rim, elevated at most by a few hundred meters above the surrounding plains, preserves unit pl materials, but nearly all other traces of the corona structure have been buried beneath the unit pr_2 and unit pr_3 materials that characterize the region. Similarly, the interior of the corona—which unlike Nimba is a depression extending almost 1 km below the surrounding plains—has been obscured by younger deposits, in this case unit fe materials (derived from the Kokyanwuti Mons edifice in the Bellona Fossae (V–15) quadrangle) that flow westward downslope across units pr_1, pr_2, and pr_3 before ponding in the low-lying corona interior.

Impact Craters

The V–14 quadrangle contains eleven impact craters, one feature which might be a twelfth impact crater (~32.2° N., 195° E.), and four airburst features (also called splotch craters); these airburst features do not create material units, but they distinctively modify the local material(s) with which they are geographically associated. Together they cover approximately 31 x 10^3 km^2 (0.5 percent of V–14), and yield an average crater density (ignoring the tentatively identified crater) of 2.3 craters per million square kilometers (without airburst features, 1.69 craters per million square kilometers). This is greater than the global average of essentially 2.0 craters per million square kilometers (see Ivanov and Basilevsky, 1993; Namiki and Solomon, 1994; Price and Suppe, 1994; Strom and others, 1994), but the difficulties inherent to efforts striving to extract dating information from these data are well documented (see Campbell, 1999). Many of the craters in the quadrangle, however, are associated with "haloes" of dark material that are often parabolic when the deposits are laterally extensive; these are indicated by a fine stippled pattern on the map. Thought to represent airfall deposits, dark halo materials are probably loosely consolidated and likely subject to weathering and erosion over time; where haloes have yet to be obliterated by weathering processes, it has been argued that deposits from the crater must be from <10 percent (parabolic) to ~70 percent (faint dark) of the mean planetary surface age (see Arvidson and others, 1992; Campbell and others, 1992; Basilevsky, 1993; Basilevsky and others, 2003). If this hypothesis is correct, then eight of the eleven craters, and presumably all of the airburst features, formed during the past few tens to hundreds of millions of years.

The craters associated with dark-halo deposits include, in order of increasing crater diameter: Lisa (D = 4.5 km; 29° N., 182° E.), Yambika (D = 6.5 km; 32.6° N., 208.7° E.), Unitkak (D = 8 km; 40.8° N., 199.5° E.), Olivia (D = 10.2 km; 37.2° N., 207.9° E.), Ugne (D = 10.3 km; 34.9° N., 205.8° E.), Uleken (D = 10.9 km; 33.7° N., 185.1° E.), Akiko (D = 17.4 km; 30.6° N., 187.3° E.), and Yablochkina (D = 64.3 km; 48.3° N., 195.3° E.). Lisa, superimposed on unit pr_2, is surrounded by ejecta deposits that extend up to 11 km from the rim and a small dark halo, with a fairly equant geometry, that extends ~45 km west from the crater center. Yambika, superimposed on unit pr_1, is surrounded by ejecta out to roughly 11 km and by a faint dark halo visible in all directions to distances of roughly 25 to 35 km from the center of the crater. In sharp contrast to Yambika, Unitkak is superimposed on unit pr_2 and has a NNW–SSE-aligned butterfly-shaped ejecta pattern that extends up to 18 km from the crater rim. This crater is also marked by a highly unusual "tail" of dark-halo materials only a few kilometers wide but extending ~600 kilometers to the west-southwest. The "tail" is clearly visible on units pr_2, pr_3, fe, and pl, and we tentatively interpret this tail, in combination with the butterfly ejecta pattern, as evidence that the impacting body passed extremely close to the surface. Specifically, the passing body approached its target at a very low impact angle, in the recent geologic past. Olivia, which impacted unit pr_3, is surrounded by an ejecta blanket out to distances of 23 km, but it shows only a faint dark halo deposit. The main region of the halo is egg-shaped, 170 km east-west by 70 km north-south, covers unit pr_3 and pr_2 materials, and like Unitkak there is also a "tail" of sorts that extends another 130 km to the west. This might also suggest a low-angle passage, but the absence of butterfly ejecta, the faintness of the dark regions, and the presence of the larger halo deposit near the crater all argue against this interpretation. We infer instead that Olivia is among the oldest dark halo craters in the quadrangle, and that the observed features are weathered remnants of what used to be a more extensive dark halo deposit. Ugne, which impacted unit pr_2 materials, is also surrounded by a faint halo, in this case equant and extending 75 to 85 km in all directions. The butterfly-shaped ejecta pattern extending 20 km from the crater rim also suggests the possibility of a low-angle impact (in this case coming in from the north, a less common trajectory), and the ejecta appears to cover lineaments and wrinkle ridges associated with Qakma Corona; along the western edge, the ejecta also appears to have abutted against pre-existing wrinkle ridge topography, implying the possibility that fluidized ejecta emplacement occurred to a limited extent. Uleken, like Ugne, is associated with a faint dark halo of limited extent (~140 km across), but for this crater the presence of fluidized ejecta emplacement is clear, and it defines a set of sinuous flows

that traverse more than 30 km across the unit pr_2 materials into which the impact occurred. The faint nature and limited extent of the haloes preserved at both Ugne and Uleken suggest that these impacts, along with Olivia, are among the oldest dark halo craters within the quadrangle. Conversely, the remaining two craters—Akiko and Yablochkina—have extensive dark halo deposits and are inferred to be, along with Unitkak, some of the youngest impact craters in the quadrangle. Akiko impacted into Lahevhev Tesserae, and while the ejecta deposits cover the structural deformation that has occurred near the impact out to distances of about 10 km the ejecta deposits, in turn, appear to be embayed or buried by intratessera plains and similar deposits within the adjacent unit pLl materials. The dark-halo deposits, parabolic in geometry, cover a variety of units (units t, pLh, pLl, pl, pr_3, pr_1, pr_2, and crater Lisa) and extend out to a distance of at least 600 km west of the crater center; however, they become fainter with increasing distance, and the deposit could extend farther because the greatest lateral extent shown in our mapping was defined conservatively. Similar criteria were used to define the parabolic dark halo deposit surrounding crater Yablochkina, which extends at least 1,270 km east-west (850 km west of the crater center) and 700 km north-south; the north-south distance is clearly a minimum as the parabola extends well into the adjacent V–5 quadrangle to the north. The dark-halo deposit covers a variety of material units (units t, pr_2, co, cof, pr_3, pl, bl, ps, ph, and fe), and unit boundaries are often more difficult to define throughout the 15 percent of the quadrangle that is affected. Crater Yablochkina is the only example in the quadrangle large enough to have formed a double-rim structure. The inner rim, 48 km across, is surrounded by an outer rim measuring 64.3 km in diameter that can be observed clearly only on the north, west, and south sides of the crater. The crater is surrounded by large ejecta blocks and fluidized deposits out to distances of 50 km from the outer rim, and these radar-bright deposits are, in turn, completely surrounded by a very low backscatter (–20.52 dB, the lowest in the quadrangle), extremely smooth deposit (RMS slope of 1.2°, lower than 98 percent of V–14's surface overall) with sharp boundaries that is distinctly separate from the dark-halo deposits; this material is mapped as unit cf. The spatial association between unit cf and the radar-bright Yablochkina ejecta suggests a link between the two. The unit has no other unusual physical properties (for example, emissivity), does not conform to topography, and we interpret this material as fine fraction flow deposits associated with Yablochkina's formation (see figure 32 in Schultz, 1992).

The three impact craters in the V–14 quadrangle that lack dark-halo deposits include, in order of increasing diameter: Clementina (D = 4 km; 35.9° N., 208.6° E.); Raymonde (D = 5.3 km; 48.4° N., 195.3° E.); and, Nadira (D = 31.4 km; 44.1° N., 201.5° E.). The absence of a dark halo deposit suggests that emplacement of each crater occurred long enough ago that weathering has had time to remove the halo deposit; we infer from the presence of haloes around small craters like Lisa that even the smallest craters likely formed a halo deposit initially. It seems likely, however, that small craters deposit less extensive and perhaps thinner dark halo deposits than large craters. If small craters do indeed have less extensive and thinner dark halo deposits, it follows that the time required to eliminate the haloes via weathering may be far less than the 10 to 70 percent inferred from study of major parabolic deposits. Clementina, slightly smaller than Lisa, impacted into unit fe materials inferred to originate from Kokyanwuti Mons in the V–15 quadrangle. The crater has a highly asymmetric ejecta deposit that extends only 1 to 2 km in most directions but up to 21 km to the south. Raymonde, which impacted into unit pr_2, is very similar, with asymmetric deposits that extend as much as 20 km from the crater rim. In contrast, Nadira is a large complex crater with a central peak, surrounded by ejecta that extend 15 km or so in all directions. The crater lies within a slightly elevated patch of unit pr_2, and it is possible that the northeast edge of the ejecta blanket, where it lies at the lowest elevation, has been covered by the unit pr_3 materials that surround the unit pr_2 materials. If this interpretation is correct, it implies that the impact postdates unit pr_2 and predates unit pr_3. The coincidence of the darker materials with a spur of higher elevation, the fairly high emissivity for the deposit (dark haloes normally have a low emissivity), and the similarity between the dark materials and nearby sections of unit pr_2 plains supports this map interpretation. An alternative and defensible interpretation, however, is that the materials mapped as unit pr_2 are misidentified and are in fact the final remnants of a dark halo deposit; this alternative interpretation would mean that Nadira impacted into unit pr_3 materials.

The final class of impact-related features present within the quadrangle is characterized by distinctively blotchy, diffuse-appearing surface modification inferred to originate when an incoming bolide fails to penetrate completely through the atmosphere, instead exploding in close proximity to, and thus disturbing, the surface without creating a crater (Schultz, 1992). The smallest, and also the least clear example of these so-called "splotch" craters (airburst features), is an irregular blotchy deposit 28 km across. It modifies unit pr_3 and is distinctly different than any materials nearby, and it is tentatively identified as an airburst product based on both its general appearance and the fine-scale flow features aligned radial to the center. The next largest splotch crater, 40 km in diameter, modifies units pr_1 and pr_2, and it is characterized by a brighter core and surrounding darker material (see figure 8c of Schultz, 1992). The third "splotch" crater, 52 km in diameter, modifies unit pr_2 materials, is circular, and contains a radar-bright pitted surface at the center. The final example, which also modifies unit pr_2 materials, is 75 km across and has a small dark center surrounded by a brighter, rougher halo of material. The sequence of unit cf materials, increasing in size, indicates variations in the efficiency with which the bolide's energy couples to the atmosphere; in other words, the greater blast areas and small dark interiors gradually transition to small, darker features with radar-bright pitted surfaces commonly observed at the core (Schultz, 1992).

Structural Deformation

The high degree of structural deformation preserved within the oldest units of the V–14 quadrangle (for example, tesserae and deformation belts) demonstrates either that these units are much more susceptible to deformation than their surroundings,

or that the early stages of the quadrangle's history involved amounts of net strain accumulation that were far greater than the deformation accommodated subsequently within the surrounding plains materials. Observed superposition and cross-cutting relations at the margins of the oldest units best support the latter interpretation but, due to the limited coverage of the old deformed areas that remain exposed, it is not possible to assess the original extent or pervasiveness of these earliest stages of deformation. Descriptions of the deformation patterns preserved within tesserae and deformation belts are provided herein; here we focus on structural deformation within the remaining material units, limiting analysis to mapped features greater than 30 km in length. We also provide a brief structural characterization of Fornax Rupes (defined by a high concentration of wrinkle ridges), Ganis Chasma (lineaments, graben, and troughs), Ahsonnutli Dorsa (lineaments and ridges) and Akawa Dorsa (lineaments and troughs), the only concentrations of deformation other than tesserae warranting a name within the quadrangle.

Contractional Deformation

Contractional deformation, in the form of wrinkle ridges (see McGill, 1993) and a handful of larger, arch-shaped ridges, occurs throughout the quadrangle. The 52 arch-shaped ridges represent a minor form of contractional deformation and never exceed 100 km in length. They have two distinctive characteristics: they are all generally aligned close to a north-south direction, and all but a handful (for example, in Ahsonnutli Dorsa) occur at the margins of elevated, highly deformed materials (for example, units bl and pl). Though these ridges are several kilometers wide, the topography of the features can be hard to detect, and the preferential north-south alignment may thus simply reflect a bias against observing linear features aligned with the approximately east-west radar look direction. In contrast to the arch-shaped ridges the wrinkle ridges in V–14, typically a few hundred meters across, represent a major form of contractional deformation within the quadrangle, and have a net length of 58,600 kilometers. Almost 80 percent of this net length occurs within regional plains units pr_2 (47 percent; these plains occupy 40.4 percent of V–14), pr_3 (17 percent; 9.3 percent of V–14), and pr_1 (15 percent; 13.1 percent of V–14); all three units contain higher than expected length percentages when compared to the percentage area they cover within the quadrangle. Their mean elevation (length-weighted; the net length for each lineament is divided into the sum of the raster cell elevation times the raster cell size for each lineament-crossed topography pixel) is 100 meters below that of the quadrangle as a whole, reflecting their preferential formation within the major plains units.

A cumulative length plot (fig. 3) illustrates that both the absolute and net lengths of contractional lineaments are about half that of the comparable figures for extensional structures within the V–14 quadrangle. No quadrangle-wide pattern of contractional deformation is observed, but regional and local patterns of alignment are evident; these patterns indicate that the most recent episodes of strain have been accommodated in different ways in different areas (Venechuk and others, 2005). In the northwest quadrant, for example, nearly all wrinkle ridges align in an east-west orientation that mirrors and contributes to the deformation that defines Akawa Dorsa. In contrast, the dense network of wrinkle ridges within the northeast quadrant, most notably expressed within unit pr_3 materials, has a northwest-southeast alignment that has no obvious relation to the topographic or other gross characteristics of the area; an exception to this occurs locally where wrinkle ridges lie immediately adjacent and parallel to the double-annulus defining the Cerridwen and Neyterkob Coronae, structures similar in scale to Akawa Dorsa. When wrinkle ridges throughout the quadrangle are summed into 15° bins (that is, alignments from N to N. 15° E., from N. 15° E. to N. 30° E.), only 5 to 12 percent of the population is aligned in each (Venechuk and others, 2005); this finding demonstrates the overall failure of the population to adopt one or more preferred orientations at the quadrangle scale.

Extensional Deformation

Extensional deformation within V–14 shows a greater variety of structural styles than is observed for contractional deformation. Minor extensional features include true graben (fault-bounded, flat-floored depressions) and troughs (wide, deep, elongated depressions without clear evidence of bounding faults). The 48 graben, with individual lengths as much as ~150 km and a net length of 3.3 thousand kilometers, are principally located within unit pG, with isolated occurrences at other locations. Their mean elevation is 300 m above that of the overall quadrangle, a fact that reflects a strong association with Ganis Chasma. Formal labeling of a feature as a graben was applied conservatively by requiring clear detection of the flat floor and faulted walls; it is possible that many features labeled as extensional lineaments could be graben as well, but their narrow widths prevent further characterization at the available radar image resolution. The 22 troughs identified also reach lengths just in excess of 150 km, but they have a net length significantly less than that of the graben (1.4 thousand kilometers). Like the graben, many troughs are observed within unit pG, but the rest are concentrated within Fornax Rupes, which leads us to infer their extensional origin.

Narrower structures defined here as lineaments are much more numerous (n=1,222) and are inferred to be extensional from their fairly uniform width and linearity across considerable distances. They are distributed in a non-uniform fashion throughout the quadrangle and extend for a net length of 71.8 thousand kilometers. Only 53 percent of this length occurs in regional plains units pr_2 (35 percent; 40.4 percent of V–14), pr_1 (16 percent; 13.1 percent of V–14), and pr_3 (2 percent; 9.3 percent of V–14), and hence the lineaments are underrepresented in these areas relative to the part of the quadrangle the units cover. Lineaments also tend to be noticeably absent from areas where abundant wrinkle ridges have formed (see unit pr_2 in northwest quadrant; unit pr_3 in northeast quadrant; and, in the units within the south-central portion of V–14), but in other areas they define concentrated patterns that clearly reflect both local and regional stress fields. For example, from 35–40° N. and 180–195° E., an organized system of lineaments runs east-west along the elevated belts of unit pl that characterize this

area, parallel to the wrinkle ridges in the immediately adjacent plains materials. Similarly, regional-scale patterns are observed defining Ganis Chasma (northwest-southeast aligned) and Fornax Rupes (northeast-southwest aligned), and lineament sets in the northeast corner of the quadrangle are aligned both parallel and perpendicular to the Neytercob and Cerridwen Coronae across distances of up to 500 km; the major perpendicular set, running northeast-southwest, creates the dominant structural character of Ahsonnutli Dorsa. Lineaments also define the circumferential deformation characterizing many other coronae and annular structures, the majority of which lie along the trace of Fornax Rupes. When lineaments throughout the quadrangle are summed into 15° bins, only 5 to 15 percent of the population is aligned in each (Venechuk and others, 2005). As was the case for the wrinkle ridges, this finding demonstrates that the lineaments population does not adopt a preferred orientation at the quadrangle scale.

The final set of extensional structures includes two sets of lineaments that radiate away from a central volcanic edifice or structure; we interpret these features as the surface expression of subsurface dikes propagating laterally at shallow depth using criteria defined by Grosfils and Head (1994a,b), but the lineaments radial to Cerridwen and Neyterkob Coronae are not included in this designation as it is not obvious that these features need be dike-underlain. The first set, consisting of 118 structures each greater than 30 km in length, radiates some 400 km across roughly 270° of arc from Xtoh Mons. The second set includes 119 structures within V–14 that radiate in total more than 1,000 km (conservatively) from Waka Mons and a volcanic center just to the southwest (Grosfils and Ernst, 2002), with some structures extending significant distances northeast into the adjacent V–15 quadrangle. These lineaments run parallel to Fornax Rupes and eventually merge with the structures defining Bellona Fossae, the feature from which V–15 derives its name, and thus this subset of northeast-striking radial features likely formed within the same stress regime (possibly at the same time as?) Bellona Fossae and Fornax Rupes. Since these radial lineaments are buried by Waka Mons deposits, which in turn are cut by other radial features from the same center that do not curve into a northeast alignment, it would appear that major (quadrangle-scale) stress patterns can be changed and/or eliminated in geologic intervals that are commensurate with the lifetime and activity at a single volcanic center. While such times are currently unconstrained for Venus volcanic centers, if these focused areas of magmatism are akin to those on Earth—a connection suggested by both the observed morphologies and the pulsed nature of the activity—then the period of time implied is likely to be on the order of a few million to at most a few tens of millions of years (see Bryan and Ernst, 2008, and references therein).

Geologic History

It is challenging to organize the stratigraphy within the quadrangle into a single comprehensive sequence due to the presence and extent of (1) the morphologically, temporally diverse "garbage bag" plains unit pr_1 that cuts several broad swaths across the quadrangle, and (2) a few extensive, crater-related, radar-dark deposits—most notably from the crater Yablochkina—which obscure stratigraphic details within parts of the quadrangle. Several clear regional sequences can be defined, however, and each stratigraphic sub-region is characterized by a common sequence of transitions from one predominant style of geological activity to another. This could indicate that each local region records a similar sequence of transitions occurring at different times and/or rates, or that some (perhaps all) local regions endured a general sequence of geologic events at about the same time and rate. In the next few sections and in the Sequence of Map Units (see map), we present the general stratigraphic sequence of units and events in the quadrangle.

Precursor

Tessera terrain t is consistently the oldest unit where it is observed as part of a local stratigraphic sequence, and the same is true for deformation belt unit bl. The relative timing of these two units is unconstrained based on the observed stratigraphy. Deformation belts are the simplest, preserved as linear elevated regions of heavily deformed material characterized by early contractional deformation and later stage extensional deformation. Tessera terrain, like deformation belts, is embayed or crosscut by all surrounding units, but its structural record has obliterated the signature of all precursor material. In no location do we observe tesserae forming at the expense of other units, though some deformation affecting tessera blocks also affects the surrounding materials. Tesserae within specific regions tend to contain similar deformation patterns (for example, the disparate blocks of Nemesis Tesserae preserve internally similar deformation), but tesserae materials from location to location within the quadrangle do not (for example, Nemesis Tesserae and Lahevhev Tesserae preserve different structural histories and stress alignments).

Period 1

A complex era of intermingled plains emplacement and distributed deformation dominated for some interval following tesserae and deformation belt formation. This era yielded two distinct types of units that locally are older than everything but the precursor materials; however, they do not occur in a consistent sequence relative to one another and instead show variable temporal relations in different areas of the quadrangle. The first type of unit consists of different plains materials cut by pervasive extensional deformation (namely, units pG, pl, pLh, and pLl) and preserved as elevated kipukas. The original extent of these units is not clearly understood because they are mostly covered by younger deposits and no source regions are apparent. The second unit type, unit pr_1 material, is at least locally the oldest feature other than tesserae and deformation belts. These plains again preserve no clear source regions and have, relative to other plains units in the quadrangle, an intermediate radar backscatter and a highly blotchy appearance suggesting they may be defined by the amalgamation of many localized (perhaps fissure) eruptions. Consistent with this, they also show high concentrations of extensional deformation relative to other

regional plains units but a fairly low concentration of contractional structures. Unit pr_1 materials display stratigraphically variable contact relationships that are often ambiguous locally but, viewed collectively, indicate the unit has undergone a prolonged history of spatially and temporally patchy emplacement and modification.

The formation of coronae in V–14, and formation of material units co and cof, also occurred predominantly during this period, although limited corona-forming activity extends into Period 2. Lineated plains units and unit pr_1 commonly are found draped upon the elevated rims that have been preserved, which indicates that these materials were emplaced prior to development of the rim topography. The rim topography was then embayed by unit pr_2 and younger deposits. While the process of corona formation and topographic development can take considerable time (Smrekar and Stofan, 1997), the observed stratigraphic details suggest that coronae are among the oldest volcanic center signatures preserved within the quadrangle. Only one corona, Madalait, has unit pr_2 plains materials on its rim, and this single example appears to be distinctly younger than the other coronae in the quadrangle.

Period 2

The next interval is characterized predominantly by extensive plains volcanism, unit pr_2; this unit preserves a similar degree of contractional deformation and a significantly lesser degree of extensional concentration than the older unit pr_1 plains materials. The unit pr_2 plains have a lower backscatter than other regional plains units, and embayment of other material units as well as the superposition locally on different lineament sets both suggest a fairly thin, possibly low viscosity deposit. Emplacement of this unit appears to have occurred over a prolonged interval and, though younger than unit pr_1 in most places, in a few places the two units are clearly overlapping. In addition to coinciding with the formation of Madalait Corona, this period is also characterized volcanicly by the formation of Baltis Vallis, which cuts unit pr_2 and is infilled locally by unit pr_3, as well as a transition from coronae to large edifice formation and initial emplacement of unit fe materials.

Period 3

The final distinct phase, which extends until the present, is characterized predominantly by edifice-related volcanism, which has formed unit fe, and emplacement of a third regional plains material, unit pr_3. Unit pr_3 is characterized by an intermediate and more uniform radar backscatter than the other plains in the quadrangle. Most of unit pr_3 occurs as a single continuous and spatially extensive unit with no evident source; onlap relations reveal this unit is thicker in the middle and thin at the edges, and unlike the older unit pr_1 and unit pr_2 plains, this broad patch appears to define a stratigraphically brief (possibly continuous?) emplacement event. Other small patches of unit pr_3 are similar in stratigraphic position, and collectively they preserve a significantly higher concentration of contractional deformation and a significantly lesser degree of extensional deformation than the older unit pr_1 and unit pr_2 materials. Complementing the unit pr_3 plains, several large (>100 km diameter) volcanoes formed and the lobate unit fe materials from these constructs are generally superimposed on the surrounding materials, including unit pr_3. Similarly, the single instance of unit ph, identified as a possible pyroclastic deposit, is younger than the units with which it comes into contact. Uncertainty remains concerning the source region for this unit, but unit ph lies at the base of a large (~900 km diameter), unnamed domical uplift. If this uplift and the other young volcanism it exhibits (abundant unit ps materials and a fanning lineament system, which may be dike-underlain) are plume related, it could indicate that one of the final major pulses of volcanic activity in the quadrangle involved volatile-rich magmas. Finally, several extensive unit ps plains characterized by overlapping small shield deposits are associated with period 3. The duration of time over which the small shields were emplaced is almost by definition unconstrained within the interior, but like unit fe, the ps units are almost everywhere younger than the materials against which they abut; the only exceptions to this are two instances of contact with unit fe and the interaction with unit ph. With clear evidence for earlier phases of small shield formation, it appears that the formation of diminutive edifices has occurred during several major stages, or perhaps persistently, throughout the quadrangle's preserved history.

Cratering

On the basis of superposition relations observed for the impact craters and their ejecta, all but one crater (Yambika) formed during or subsequent to period 2, the era of unit pr_2 plains emplacement, and nearly half of the craters formed in period 3 during or after the emplacement of unit pr_3. Only one crater, Nadira, has been embayed since it formed, hence placing an upper bound on its time of formation. The remainder must be younger than the units into which they impacted and onto which their dark halo deposits and ejecta were deposited, but no further constraint based on superposition is possible. As discussed previously, however, most craters in the quadrangle preserve dark halo deposits to some degree (italicized craters shown on the Sequence of Map Units are the exceptions to this); the lack of dark halo deposits suggest that these craters may have formed within the last few tens to hundreds of millions of years.

Discussion

Mapping within the V–14 quadrangle, as noted in the Introduction, was performed to yield insight into four specific questions.

> *Question 1*: Has the dominant style of volcanic expression within the quadrangle varied in a systematic fashion over time?

There is a clearly preserved variation in volcanic style within the V–14 quadrangle, and it suggests a processional volcanic sequence. We also hypothesize that the precursor materi-

als from which tesserae and deformation belt units have formed were volcanic as well, but there are no mapping constraints suitable at present for testing this hypothesis.

Stratigraphically early plains formation and the emplacement of small shields dominate the bulk of the stratigraphy exposed; evidence for the latter is now largely preserved adjacent to and upon kipukas within the most elevated regional plains units. The oldest units are generally the most heavily deformed, and in many places they were uplifted during corona-forming processes that prevented the units' subsequent burial when younger plains materials were erupted onto the surface. The interplay between structural and material unit elements preserved at some coronae make it clear that activity at these magmatic centers continued over a prolonged period. The coronae characteristics observed within V–14 are consistent with their genesis during delamination events affecting a thin lithosphere (Smrekar and Stofan, 1997), but the observed morphologies and ages do not support other proposed models of corona formation (see DeLaughter and Jurdy, 1999).

In the later stages of the quadrangle's evolution, small shield emplacement continued to form the mapped units of ps, but the style of volcanism otherwise largely appears to have localized into edifice formation at distinct centers of activity; the gradual but clear transition from corona- to large edifice-dominated construction at volcanic centers is consistent with predictions involving gradual lithospheric thickening over time (see McGovern and Solomon, 1998). The duration of activity at individual large edifices is poorly constrained, but it is clear that the latest activity at essentially all of the large volcanoes, based on superposition and crosscutting relations of materials mapped as unit fe with their surroundings, postdates the most recent activity in adjacent units. Interestingly, in addition to the geologically recent effusive growth at large edifices, the characteristics of unit ph indicate that late-stage activity in at least one area of the quadrangle, adjacent to a large, unnamed domical volcanic rise 900 km across, may have involved explosive eruption of magmas with an extremely high volatile content.

In addition to effusive and possibly explosive activity, careful evaluation of the volcanic, tectonic and topographic evolution of two extensive, edifice-centered radial fracture systems using techniques defined previously (Grosfils and Head, 1994a,b) provides insight into a third major style of late-stage volcanic activity within V–14: subsurface emplacement of giant radiating dike systems. The dikes in each radial system are inferred, from the combination of observations, to have injected laterally away from a shallow magma source. Calculations indicate that the magma reservoirs associated with each source were likely to be a few tens of kilometers in plan-view radius, and that the dikes fed from these reservoirs would need to be a few tens of meters across (Grosfils and Ernst, 2002). The rapidity with which individual dikes are emplaced (days to a week or two for dikes ~1,000 km long given thermal- and fluid-dynamic limitations on dike growth; Ernst and others, 1995) make these features excellent stratigraphic tie points. The interplay between the dike-induced lineaments seen at the surface and the material units with which they interact indicates that thermal and hence volcanic activity at both centers reoccurred during several distinct episodes over a stratigraphically prolonged interval.

Question 2: Does the tectonic deformation within the quadrangle record significant regional patterns that vary spatially or temporally, and if so what are the scales, orientations, and sources of the stress fields driving this deformation?

Analysis of the structural styles preserved within the quadrangle indicates that significant and fairly systematic changes have occurred as a function of time (see Sequence of Map Units). The earliest phases of structural deformation in the quadrangle (for example, those forming units t and bl) are predominantly contractional. Following this interval, the oldest plains units preserved are characterized by significant degrees of extensional deformation but only limited contraction; correlation between the development of early stages of volcanism and a period of enhanced extension may not be accidental. As volcanic activity within the quadrangle continued, however, it gradually led to the emplacement of the major regional plains, and contractional deformation once again came to dominate the structural signatures observed; this interval of variation corresponds to the gradual shift from regional plains emplacement to localized centers of activity. Finally, the nature of the most recent stress fields in the area is generally unconstrained because the stratigraphically youngest units preserve only limited amounts of structural deformation.

Spatial analysis of tectonic deformation within V–14 as a whole does not reveal a quadrangle-wide pattern of spatial deformation but rather discrete zones, roughly one fifth to one-fourth the area of the quadrangle in size, that have distinctive tectonic patterns. Quantitative analysis of the lineaments in these zones in some cases reveals clear evidence of structural organization across wide areas. For instance, within a zone stretching across the northern part of the quadrangle (~2 x 10^{12} km^2), suites of extensional and contractional lineaments show clear orthogonality (Venechuk and others, 2005). This characteristic may indicate that the tectonic deformation occurred during a geologically brief interval, or it could indicate that the structures formed in the presence of a long-lived, persistently aligned regional stress field. A similarly orthogonal pattern (requiring regional stress fields aligned in a very different direction from the northern area) occurs in the southwest part of V–14. In other areas of the quadrangle, in contrast, extensional and contractional lineaments are aligned sub-parallel to each other or lack coherent geometric organization; these observations indicate variability in stress field alignment over time and/or possible reactivation of individual structural elements. Reactivation has been observed in other regions (see DeShon and Hansen, 2000).

Stratigraphically, combining the temporal and spatial characteristics, there is a general sequence preserved in which the oldest units show the most deformation and the youngest units the least; however, specific units fall outside these patterns, which suggests deformation concentration has occurred at some level. There are several possible interpretations of these data. The most obvious one is that enhanced extensional deformation occurred across the region during the interval of emplacement represented by the units coeval with and predating plains unit pr_1, with lesser degrees of extension thereafter; enhanced

levels of contractional deformation within late-stage plains units largely appear to reflect accommodation of pre-existing topography. Another possibility, but one we consider less viable on the basis of the map data, is that the process of deformation took place after emplacement of most material units, with little deformation occurring in some materials and hence preferential concentration of structural features within what are now the most heavily deformed plains units. These more deformed areas remain the stratigraphically oldest, which would suggest that some factor, perhaps related to their pre-existing stress or thermal state, their material properties, or their thickness is fundamentally different than the properties of the younger plains-forming materials.

The current mapping effort does not concentrate heavily upon the structural deformation recorded within tesserae, but the structural data and geologic history preserved within these units yield insight into early- and late-stage deformation within the quadrangle, and each area has its own particular geologic character. Nemesis Tesserae form an elongate belt that cuts east-west across the north-central part of the quadrangle. It is preserved as elevated kipukas that have been embayed by surrounding plains units, and there is no progression of deformation observed; for example, structures that systematically deform both the tessera blocks and parts of the surrounding plains are absent. Deformation within this tessera terrain was essentially complete by the time the surrounding plains and topography were emplaced. In contrast, the Athena Tesserae occur as an equant block (contained mostly within V–13 to the west) that exhibits interplay between tectonic deformation, plains emplacement, and uplift. For example, along the eastern edge of the quadrangle (31.5° N., 182° E.), the tessera was embayed by plains deposits, then both the plains and tessera apparently underwent an episode of structural deformation perpendicular to the embayment boundary that cut across them both to form unit pl. The contact between the two material units was subsequently uplifted, and a second plains emplacement event, which formed unit pr_1, embayed both the structural lineaments and the older plains unit where they occurred at lower elevations. Following continued uplift, emplacement of unit pr_2 materials in the lowest lying areas occurred. This event is an example where late-stage tectonic deformation of the tessera was coeval with early regional plains emplacement, while later plains emplacement events occurred during an interval of ongoing topographic adjustment. Finally, the Lahevhev Tesserae appear to be the remnants of a larger coherent block of tessera which is in (or ceased deforming during) the process of being torn apart by tectonic and volcanic activity. The inferred block is cut in several places by rift-like topography within which flooding and subsequent development of lineaments with a braided and/or feathery geometry has occurred, potentially indicative of local shearing. The larger coherent blocks of tessera preserved within Lahevhev Tesserae resemble Nemesis Tesserae in that their internal deformation is clearly not coeval with emplacement of the surrounding plains.

Given the changes in tectonic deformation that are observed in units of different stratigraphic ages, it would be useful to constrain the spatial extent across which the stress fields are capable of varying and the rate at which major stress configurations can change. Within V–14, the most useful tools for both aspects are the radial dike systems associated with Waka Mons and Asintmah Corona. Emplaced rapidly, and with alignments dictated by the stress state of the crust, such dikes are stratigraphic markers that yield powerful insight into the spatial alignment of tectonic stresses within the dike-intruded region at the time the dikes were emplaced. Within 300–500 km or so of their geographic center the dikes are gently arcuate, but beyond that they have clearly been influenced by local stress concentrations. Within V–14, north of their origin, the dikes swing one way and then another in response to stress concentrations at different coronae and paterae (for example, see the deflections occurring near 33.5° N., 206.5° E.), while beyond V–14, further to the northeast, the dikes concentrate into a narrow belt of deformation aligned with Bellona Fossae, for which the V–15 quadrangle is named. The dikes are thus highly useful for understanding areas in which regional tectonic forces dominate (for example, Bellona Fossae), and those where such stresses are minimal leaving the stress field geometries to be defined by local stress concentrators (for example, between coronae). Constraining the rate at which stress fields can change is more difficult given existing data, but some insights can still be gained from the Waka/Asintmah dike swarms. The major radial elements, extending considerable distances while adopting alignments sub-parallel to both Fornax Rupes (V–14) and Bellona Fossae (V–15), are subsequently buried by lava flows from Waka Mons. These flows in turn are cut by younger radial dikes with geometries that do not reflect the presence of the regional-scale stress field responsible for producing Fornax Rupes and Bellona Fossae. While this does not resolve the uncertainty about the rates at which major stress fields can change, it does suggest that the time frame required is commensurate with the duration of activity at a major volcanic center. Based on data from similar systems on Earth, this suggests that major stress patterns across the region may be capable of changing on time frames of a few to at most a few tens of millions of years.

> *Question 3*: If mantle upwelling and downwelling have played a significant role in the formation of Atla Regio and Atalanta Planitia as has been proposed, does the geology of Ganiki Planitia record evidence of northwest-directed lateral mantle flow connecting the two sites?

The V–14 quadrangle lies between the Atla Regio domical highland, an area to the SSE inferred to be a site of active mantle upwelling, and the Atalanta Planitia lowlands to the northwest, which some have interpreted to be a product of mantle downwelling. An explicit goal of this mapping project was to determine whether or not there is a regional tectonic signature within the quadrangle that suggests the presence of lateral mantle flow connecting Atla and Atalanta, a process which would be expected to generate (broadly) extensional deformation parallel to the flow (that is, roughly NNW) and contractional deformation orthogonal to this direction (that is, roughly ENE).

Analysis of all mapped lineaments (excluding those within the tessera terrains) does not reveal a quadrangle-wide pat-

tern indicative of the hypothesized lateral mantle flow, and, accordingly, there is no evidence to support the idea that the two regions, Atla and Atalanta, are or were dynamically linked. There are several possible implications. First, since Atla is a modern center of upwelling, it is possible that stresses induced by mantle flow outward from Atla have not yet had sufficient time to manifest as tectonic deformation in V–14. This seems unlikely, however, given the magnitude of the plume-related volcanic and tectonic activity in the Atla region, and the probability that activity in this site, though currently ongoing, has been long-lived (see Basilevsky, 1993). A second possibility is that mantle flow away from the Atla site is preferentially channeled into a specific direction, perhaps by inverted topographic variations along the base of the crust/lithosphere. One example that seems possible is flow along the course of the rift systems that cut Atla, which one would expect to look somewhat necked in cross section and which may therefore provide channels for preferential mantle flow away from the center of plume upwelling. Available gravity and radar data are currently insufficient to test this hypothesis rigorously. Third, it is possible that Atalanta is a relict downwelling location, meaning that flow out and away from Atla is not in any special sense directed toward the Atalanta site. Finally, it is possible that Atalanta is not (and was not) a site of downwelling, namely, that it formed via other means.

Question 4: Does integration of the tectonic and volcanic histories preserved within the quadrangle help constrain competing resurfacing models for Venus?

Exploring whether or not the surface of Venus records evidence for catastrophic resurfacing, or if it was resurfaced in a uniformitarianism fashion, requires a global-scale synthesis and interpretation of the stratigraphy that has been preserved. No mapping effort in a single quadrangle-sized area can address this question definitively. However, it is the amalgamation of observations from individual quadrangles that will yield the data necessary to address the matter, and the hope is that stand-alone results from individual areas like V–14 will provide insight into which hypothesis is most strongly supported. Here we summarize the key components—cratering data and unit stratigraphy—from within the V–14 quadrangle below.

There are eleven confirmed impact craters in V–14, which yields a net crater density of approximately 1.68 per million square kilometers, well below the global average of ~2 craters per million square kilometers. The small number of craters calls into question the validity of inferring any sort of relative age from these data, but other aspects of the cratering record, such as the presence of dark-halo materials, prove more useful.

While only one crater in the quadrangle, Yablochkina, is associated with a massive parabolic deposit, many others are surrounded by diffuse radar-dark deposits akin to the larger parabolic deposit of Yablochkina. In addition, the small crater Unitkak is associated with a spectacular long (~600 km), narrow (tens of kilometers) radar dark streak, which we infer to be possible evidence for a low-angle trajectory event. Of the remaining craters, Raymonde lies close to Yablochkina and within its parabolic deposit, and this relation prevents clear identification of any such signature from Raymonde alone; Clementina is not associated with any radar-dark deposits; and Nadira is the only crater that has been modified subsequent to emplacement as it has been embayed by flows of the youngest regional plains unit pr_3. Erosion/weathering time hypothesized to remove diffuse, radar-dark deposits like the parabolas and similar features is predicted to be a few tens to hundreds of millions of years, which suggests the bulk of the cratering in the region may be disproportionately young, and which, in turn, suggests a younger bulk age for the quadrangle than is inferred from the crater density alone.

The material unit stratigraphy within the quadrangle is difficult to organize into a single comprehensive sequence, but a common sequence of transitions from one predominant style of geologic activity to another is observed. Critically, there are (a) no locations where tesserae are not the oldest unit preserved (if they exist in the area), and (b) no locations where evidence of "overlap zones" occur, that is places where one region's tesserae (or other stratigraphically older unit) is forming at the expense of a stratigraphically younger unit in the same sequence from another area in an unexpected fashion. Put another way, there is no evidence to suggest that the common stratigraphies observed in the different regions formed at different times, although it is impossible to eliminate this possibility. Taken together, these data could indicate that each local region records a similar sequence of transitions occurring at different times and/or rates, or that some/all of the local regions endured a general sequence of geologic events at about the same time and rate. To gain better insight into proposed resurfacing models requires integration of Ganiki Planitia quadrangle's geologic record with those for the surrounding areas.

Acknowledgments

This research was primarily funded by grant NAG5-10157 from NASA's Planetary Geology and Geophysics Program, with additional support from the Planetary Geology and Geophysics Undergraduate Research Program and Pomona College's Summer Undergraduate Research Program. We are grateful to Misha Ivanov, Jim Head, Nick Lang, Carolyn Donlin, Trent Hare, Jennifer Blue, and Ken Tanaka for their thorough reviews and insightful comments. As the dust settled on this project, a group of undergraduates who worked on the project for several years and contributed in a significant fashion became co-authors, but many other undergraduate students were involved in the project over the years, and I offer my thanks to Madalyn Blondes, Thomas Doggett, Warren Katzenstein, Nobu Koch, Zach Miller, Nissa Morton, Scott Pelletier, Anjani Polit, and Alice Waldron. As first author, I am grateful to everyone who has been involved; the interactions we shared certainly kept this research endeavor stimulating and fun!

References

Arvidson, R.E., Greeley, R., Malin, M.C, Saunders, R.S., Izenberg, N., Plaut, J.J., Stofan, E.R., and Shepard, M.K., 1992,

Surface modification of Venus as inferred from Magellan observation of plains: Journal of Geophysical Research, v. 97, p. 13,303–13,317.

Baker, V.R., Komatsu, G., Parker, T.J., Gulick, V.C, Kargel, J.S., and Lewis, J.S., 1992, Channels and valleys on Venus: Characteristics, geologic setting, and eruption conditions from Magellan data: Journal of Geophysical Research, v. 97, p. 13,421–13,444.

Banfield, J.D., and Raftery, A.E., 1993, Model-Based Gaussian and Non-Gaussian Clustering: Biometrics, v. 49, no. 3, p. 803–821.

Barnett, D.N., Nimmo, F., and McKenzie, D., 2002, Flexure of Venusian lithosphere measured from residual topography and gravity: Journal of Geophysical Research, v. 107, no. E2, doi:10.1029/2000JE001398.

Basilevsky, A.T., 1993, Age of rifting and associated volcanism in Atla Regio, Venus: Geophysical Research Letters, v. 20, p. 883–886.

Basilevsky, A.T., and Head, J.W., 1995, Global stratigraphy of Venus: Analysis of a random sample of thirty-six test areas: Earth Moon Planets, v. 66, p. 285–336.

Basilevsky, A.T., and Head, J.W., 1996, Evidence for rapid and widespread emplacement of volcanic plains on Venus: Stratigraphic studies in the Baltis Vallis region: Geophysical Research Letters, v. 23, no. 12, p. 1,497–1,500.

Basilevsky, A.T., and Head, J.W., 1998, The geologic history of Venus: A stratigraphic view: Journal of Geophysical Research, v. 103, no. E4, p. 8,531–8,544.

Basilevsky, A.T., and Head, J.W., 2000, Geologic units on Venus: evidence for their global correlation: Planetary and Space Science, v. 48, no. 1, p. 75–111.

Basilevsky, A.T., and Head, J.W., 2002, On rates and styles of late volcanism and rifting on Venus: Journal of Geophysical Research, v. 107, no. E6, doi:10.1029/2000JE001471.

Basilevsky, A.T., Head, J.W., and Setyaeva, I.V., 2003, Venus: Estimation of age of impact craters on the basis of degree of preservation of associated radar-dark deposits: Geophysical Research Letters, v. 30, no. 18, doi:10.1029/2003GL017504.

Bilotti, F., and Suppe, J., 1999, The global distribution of wrinkle ridges on Venus: Icarus, v. 139, no. 1, p. 137–157.

Bindschadler, D.L., Schubert, G., and Kaula, W.M., 1992, Coldspots and hotspots: Global tectonics and mantle dynamics of Venus: Journal of Geophysical Research, v. 97, p. 13,495–13,532.

Bray, V.J., Bussey, D.B.J., Ghail, R.C, Jones, A.P., and Pickering, K.T, 2007, Meander geometry of Venusian canali: Constraints on flow regime and formation time: Journal of Geophysical Research, v. 112, no. E4, doi:10.1029/2006JE002785.

Brian, A.W., Stofan, E.R., and Guest, J.E., 2005, Geologic Map of the Taussig Quadrangle (V–39), Venus: U.S. Geological Survey Scientific Investigations Map 2813.

Bryan, S.E., and Ernst, R.E., 2008, Revised definition of large igneous provinces (LIPs): Earth-Science Reviews, v. 86, no. 1–4, p. 175–202.

Burba, G.A., Blue, J., Campbell, D.B., Dollfus, A., Gaddis, L., Jurgens, R.F., Marov, M.Y., Pettengill, G.H., and Stofan, E.R., 2001, Venus nomenclature: Progress in 2000, triennial report for 1997–2000, current state and prospective: Lunar and Planetary Science Conference, Abstract #2098 (CD-ROM), v. XXXII.

Campbell, B.A., 1995, Use and presentation of Magellan quantitative data in Venus mapping: U.S. Geological Survey Open-File Report 95-519, 32 p.

Campbell, B.A., 1999, Surface formation rates and impact crater densities on Venus: Journal of Geophysical Research-Planets, v. 104, no. E9, p. 21,951–21,955.

Campbell, B.A., Glaze, L., and Rogers, P.G., 1998, Pyroclastic deposits on Venus: Remote-sensing evidence and modes of formation: Lunar and Planetary Science Conference, Abstract #1810 (CD-ROM), v. XXIX.

Campbell, D.B., Stacy, N.J.S., Newman, W.I., Arvidson, R.E., Jones, E.M., Musser, G.S., Roper, A.Y., and Schaller, C, 1992, Magellan observations of extended impact crater related features on the surface of Venus: Journal of Geophysical Research, v. 97, p. 16,249–16,278.

Crumpler, L.S., and Aubele, J.C, 2000, Volcanism on Venus, *in* Sigurdsson, H., Houghton, B., McNutt, S., Rymer, H., and Stix, J., eds., Encyclopedia of Volcanoes: San Diego, Academic Press, p. 727–769.

Crumpler, L.S., Head, J.W., and Aubele, J.C, 1993, Relation of major volcanic center concentration on Venus to global tectonic patterns: Science, v. 261, p. 591–595.

DeLaughter, J.E., and Jurdy, D.M., 1999, Corona classification by evolutionary stage: Icarus, v. 139, p. 81–92.

Dempster, A.P., Laird, N.M., and Rubin, D.B., 1977, Maximum likelihood from incomplete data via EM algorithm: Journal of the Royal Statistical Society Series B-Methodological, v. 39, no. 1, p. 1–38.

DeShon, H.R., Young, D.A., and Hansen, V.L., 2000, Geologic evolution of southern Rusalka Planitia, Venus: Journal of Geophysical Research, v. 105, no. E3, p. 6,983–6,995.

Ernst, R.E., Head, J.W., Parfitt, E., Grosfils, E.B., and Wilson, L., 1995, Giant radiating dyke swarms on Earth and Venus: Earth Science Reviews, v. 39, p. 1–58.

Ford, J.P., Blom, R.G., Crisp, J.A., Elachi, C, Farr, T.G., Saunders, R.S., Theilig, E.E., Wall, S.D., and Yewell, S.B., 1989, Spaceborne Radar Observations: A Guide for Magellan Radar-Image Analysis: JPL Publication 89-41, 126 p.

Ford, J.P., Plaut, J.J., Weitz, C.M., Farr, T.G., Senske, D.A., Stofan, E.R., Michaels, G., and Parker, T.J., 1993, Guide to Magellan Image Interpretation: JPL Publication 93-24, 148 p.

Ford, P.G., and Pettengill, G.H., 1992, Venus topography and kilometer-scale slopes: Journal of Geophysical Research, v. 97, p. 13,103–13,114.

Fraley, C, and Raftery, A.E., 2002, Model-based clustering, discriminant analysis, and density estimation: Journal of the American Statistical Association, v. 97, no. 458, p. 611–631.

Frank, S.L., and Head, J.W., 1990, Ridge belts on Venus: Morphology and origin: Earth Moon Planets, v. 50/51, p. 421–470.

Gregg, T.K., and Greeley, R., 1993, Formation of Venusian canali: Considerations of lava types and their thermal

behaviors: Journal of Geophysical Research, v. 98, p. 10,873–10,882.
Grosfils, E.B., Aubele, J.C, Crumpler, L.S., Gregg, T.K.P., and Sakimoto, S.E.H., 2000, Volcanism on Earth's seafloor and Venus, *in* Zimbelman, J.R., and Gregg, T.K.P., eds., Environmental Effects on Volcanic Eruptions: From Deep Oceans to Deep Space: New York, Plenum Publishing, p. 113–142.
Grosfils, E.B., and Ernst, R.E., 2002, Two radiating dike swarms in the Nemesis Tessera quadrangle (V–14) on Venus: Lunar and Planetary Science Conference, Abstract #1102 (CD-ROM), v. XXXIII.
Grosfils, E.B., and Head, J.W., 1994a, Emplacement of a radiating dike swarm in western Vinmara Planitia, Venus: Interpretation of the regional stress field orientation and subsurface magmatic configuration: Earth Moon Planets, v. 66, p. 153–171.
Grosfils, E.B., and Head, J.W., 1994b, The global distribution of giant radiating dike swarms on Venus: Implications for the global stress state: Geophysical Research Letters, v. 21, p. 701–704.
Guest, J.E., and Stofan, E.R., 1999, A new view of the stratigraphic history of Venus: Icarus, v. 139, no. 1, p. 55–66.
Hansen, V.L., 2000, Geologic mapping of tectonic planets: Earth and Planetary Science Letters, v. 176, no. 3–4, p. 527–542.
Hansen, V.L., 2005, Venus's shield terrain: Geological Society of America Bulletin, v. 117, no. 5–6, p. 808–822.
Ivanov, B.A., Nemchinov, I.V., Svetsov, V.A., Provalov, A.A., Khazins, V.M., and Phillips, R.J., 1992, Impact cratering on Venus: Physical and mechanical models: Journal of Geophysical Research, v. 97, p. 16,167–16,182.
Ivanov, M.A., and Basilevsky, A.T, 1993, Density and morphology of impact craters on tessera terrain, Venus: Geophysical Research Letters, v. 20, p. 2,579–2,582.
Ivanov, M.A., and Head, J.W., 1996, Tessera terrain on Venus: A survey of the global distribution, characteristics, and relation to surrounding units from Magellan data: Journal of Geophysical Research, v. 101, no. E6, p. 14,861–14,908.
Ivanov, M.A., and Head, J.W., 1999, Stratigraphic and geographic distribution of steep-sided domes on Venus: Preliminary results from regional geological mapping and implications for their origin: Journal of Geophysical Research, v. 104, no. E8, p. 18,907–18,924.
Ivanov, M.A., and Head, J.W., 2001, Geology of Venus: Mapping of a global geotraverse at 30 degrees N latitude: Journal of Geophysical Research, v. 106, no. E8, p. 17,515–17,566.
Ivanov, M.A., and Head, J.W., 2004, Stratigraphy of small shield volcanoes on Venus: Criteria for determining stratigraphic relationships and assessment of relative age and temporal abundance: Journal of Geophysical Research, v. 109, no. E10, doi:10.1029/2004JE002252.
Ivanov, M.A., and Head, J.W., 2005, Geologic Map of the Nemesis Tesserae Quadrangle (V–13), Venus: U.S. Geological Survey Scientific Investigations Map 2870.
Kirk, R.L., Soderblom, L.A., and Lee, E.M., 1992, Enhanced visualization for interpretation of Magellan radar data: Supplement to the Magellan Special Issue: Journal of Geophysical Research, v. 97, p. 16,371–16,380.
Konopliv, A.S., Banerdt, W.B., and Sjogren, W.L., 1999, Venus gravity: 180th degree and order model: Icarus, v. 139, no. 1, p. 3–18.
Konopliv, A.S., and Sjogren, W.L., 1994, Venus spherical harmonic gravity model to degree and order 60: Icarus, v. 112, no. 1, p. 42–ß54.
Lang, N.P., and Hansen, V.L., 2006, Venusian channel formation as a subsurface process: Journal of Geophysical Research, v. 111, no. E4, doi:10.1029/2005JE002629.
Long, S.M., and Grosfils, E.B., 2004, Potential pyroclastic deposit in the Nemesis Tessera (V–14) quadrangle of Venus: Lunar and Planetary Science Conference, Abstract #1194 (CD-ROM), v. XXXV.
Long, S.M., and Grosfils, E.B., 2005, Quantitative analysis of Venus radar backscatter data in ArcGIS: Lunar and Planetary Science Conference, Abstract #1032 (CD-ROM), v. XXXVI.
McGill, G.E., 1993, Wrinkle ridges, stress domains, and kinematics of Venusian plains: Geophysical Research Letters, v. 20, p. 2,407–2,410.
McGovern, P.J., and Solomon, S.C, 1998, Growth of large volcanoes on Venus: Mechanical models and implications for structural evolution: Journal of Geophysical Research, v. 103, p. 11,071–11,102.
McKenzie, D., 1994, The relationship between topography and gravity on Earth and Venus: Journal of Geophysical Research, v. 112, p. 55–88.
Namiki, N., and Solomon, S.C, 1994, Impact crater densities on volcanoes and coronae on Venus: Implications for volcanic resurfacing: Science, v. 265, p. 929–933.
Nimmo, F., and McKenzie, D., 1998, Volcanism and tectonics on Venus: Annual Review of Earth and Planetary Sciences, v. 26, p. 23–51.
Phillips, R.J., and Hansen, V.L., 1998, Geological evolution of Venus: Rises, plains, plumes, and plateaus: Science, v. 279, p. 1,492–1,497.
Price, M., and Suppe, J., 1994, Young volcanism and rifting on Venus: Nature, v. 372, p. 756–759.
Richards, J.W., Hardin, J. and Grosfils, E.B., 2010, Weighted model-based clustering for remote sensing image analysis: Computational Geosciences, v. 14, p. 125–136.
Rosenberg, E., and McGill, G.E., 2001, Geologic Map of the Pandrosos Dorsa Quadrangle (V–5), Venus: U.S. Geological Survey Open Geologic Investigations Series I–2721.
Schultz, P.H., 1992, Atmospheric effects on ejecta emplacement and crater formation on Venus from Magellan: Journal of Geophysical Research, v. 97, p. 16,183–16,248.
Smrekar, S., 1994, Evidence for active hotspots on Venus from analysis of Magellan gravity data: Icarus, v. 112, p. 2–26.
Smrekar, S.E., Comstock, R., and Anderson, F.S., 2003, A gravity survey of Type 2 coronae on Venus: Journal of Geophysical Research, v. 108, no. E8, doi:10.1029/2002JE001935.
Smrekar, S.E., and Stofan, E.R., 1997, Corona formation and heat loss on Venus by coupled upwelling and delamination:

Science, v. 277, no. 5330, p. 1,289–1,294.
Smrekar, S.E., and Stofan, E.R., 2003, Effects of lithospheric properties on the formation of Type 2 coronae on Venus: Journal of Geophysical Research, v. 108, no. E8, doi:10.1029/2002JE001930.
Stofan, E.R., Smrekar, S.E., Tapper, S.W., Guest, J.E., and Grindrod, P.M., 2001, Preliminary analysis of an expanded corona database for Venus: Geophysical Research Letters, v. 28, no. 22, p. 4,267–4,270.
Strom, R.G., Schaber, G.G., and Dawson, D.D., 1994, The global resurfacing of Venus: Journal of Geophysical Research, v. 99, p. 10,899–10,926.
Tanaka, K.L., 1994, The Venus Geologic Mappers' Handbook: U.S. Geological Survey Open File Report 94-438, p. 1–68.
Venechuk, E.M., Hurwitz, D.M., Drury, D.E., Long, S.M., and Grosfils, E.B., 2005, Analysis of tectonic lineaments in the Ganiki Planitia (V–14) quadrangle, Venus: Lunar and Planetary Science Conference, Abstract #1047 (CD-ROM), v. XXXVI.
Waldron, A.C, Blondes, M.S., Katzenstein, W.P., and Grosfils, E.B., 2003, Geologic map interpretations of the surface of the Nemesis Tessera (V–14) quadrangle, Venus: Lunar and Planetary Science Conference, Abstract #1060 (CD-ROM), v. XXXIV.
Waltham, D., Pickering, K.T, and Bray, V.J., 2008, Particulate gravity currents on Venus: Journal of Geophysical Research, v. 113, no. E2, doi:10.1029/2007JE002913.
Wilhelms, D.E., 1990, Geologic Mapping, *in* Greeley, R., and Batson, R.M., eds., Planetary Mapping: New York, Cambridge University Press, p. 208–260.
Zuber, M.T, 1987, Constraints on the lithospheric structure of Venus from mechanical models and tectonic surface features: Journal of Geophysical Research, v. 92, p. E541–E551.

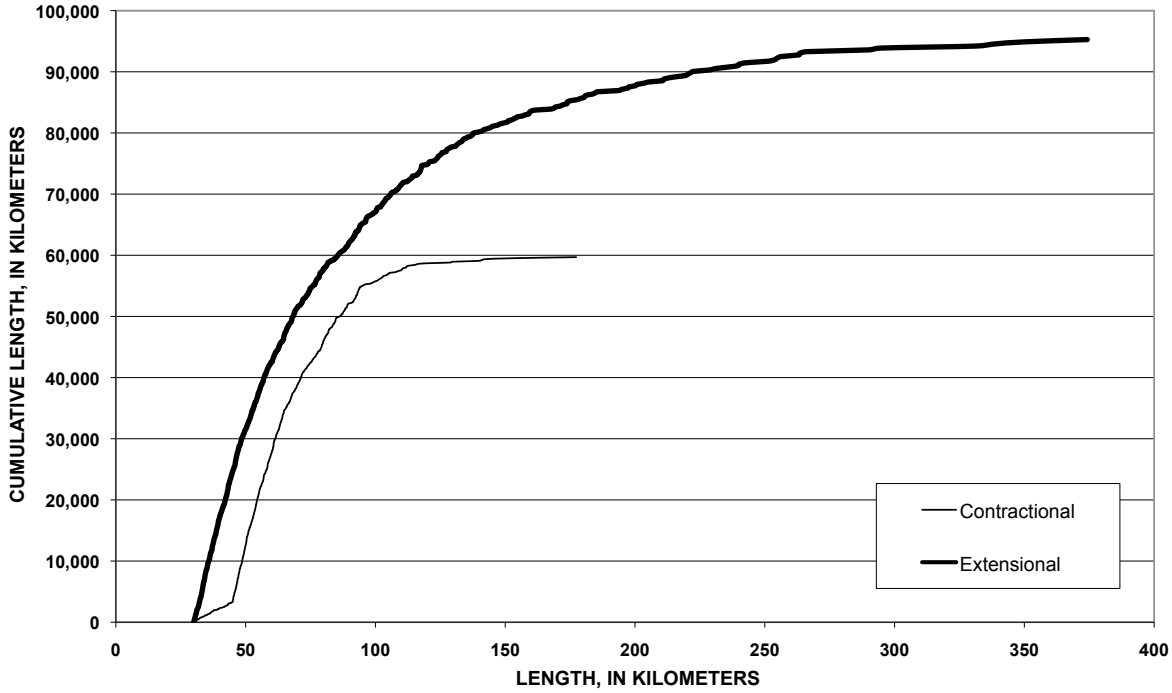

Figure 3. Cumulative length plots depicting extensional (heavy line) and contractional (lighter line) structures in V–14; only features greater than 30 km in length (that is, largely those shown on the map) are depicted. There are far more extensional lineaments than contractional, both in net and at any given structural length, and the absolute length achieved by individual extensional features is roughly twice that of the longest contractional features. Extensional deformation, occurring mostly during the early- to middle-stages of the quadrangle's stratigraphic evolution, is the dominant outcome for this scale of tectonic deformation in the V–14 quadrangle

Table 1. Summary of map unit properties within Ganiki Planitia (V–14) quadrangle, Venus.
[dB, decibels; RMS root mean square; deg, degrees]

Symbol	Area (km^2)[1]	Backscatter_Adj (dB)	Topography (km)[2]	Emissivity	Reflectivity	RMS Slope (deg)
V14	**6,583,792**	**–15.79**	**0.00**	**0.874**	**0.111**	**2.80**
bl	55,095	–15.24	0.23	0.885	0.100	3.46
c	20,157	–13.24	–0.34	0.866	0.137	2.21
cf	9,856	–20.52	–0.13	0.851	0.175	1.15
co	34,147	–15.69	0.08	0.880	0.121	3.64
cof	58,389	–15.05	–0.18	0.880	0.117	2.79
fe	655,409	–14.69	–0.03	0.880	0.104	2.70
pG	156,863	–12.08	0.62	0.892	0.084	3.77
ph	14,811	–19.45	0.34	0.916	0.084	4.31
pl	333,143	–14.28	0.11	0.887	0.091	3.13
pLh	12,547	–12.21	–0.05	0.906	0.066	5.00
pLl	145,969	–12.41	0.39	0.891	0.073	3.44
pr_1	861,323	–13.62	0.18	0.889	0.087	3.08
pr_2	2,660,025	–17.84	–0.11	0.863	0.127	2.45
pr_3	611,665	–15.46	–0.45	0.863	0.128	2.65
ps	552,131	–16.36	0.04	0.874	0.110	2.78
t	391,217	–12.31	0.43	0.903	0.081	4.01

[1]All values reflect area-normalized calculations; the area modified by airburst craters covers another 11,000 km^2.
[2]All topography values given relative to the mean elevation for V–14 quadrangle or 6,051.58 km.

Table 2. Individual map unit properties and names for every geographically distinct example of each unit, arranged alphabetically by map symbol and then by increasing area. Each entry in the table corresponds to a single discrete example (for example, closed polygon) of the unit. The unit latitude and longitude provided for each table entry is the centroid location calculated within ArcGIS.

Symbol	Lat (deg N)	Long (deg E)	Area (km^2)	Backscatter_Adj (dB)		Topography (km)[a]		Emissivity		Reflectivity		RMS Slope (deg)		IAU Name[1]
				Mean	1 Sigma	Mean	1 Sigma	Mean	1 Sigma	Mean	1 Sigma	Mean	1 Sigma	
bl	44.46	195.72	4,459	–17.58	3.97	0.55	0.30	0.881	0.008	0.106	0.022	2.99	1.23	
bl	43.94	192.10	5,164	–17.46	3.75	0.78	0.26	0.870	0.010	0.120	0.007	2.66	0.35	
bl	41.05	192.98	8,363	–12.87	2.71	0.25	0.17	0.894	0.009	0.093	0.007	3.65	0.92	
bl	41.05	196.00	11,382	–14.02	2.73	0.21	0.22	0.886	0.011	0.102	0.014	3.79	1.09	
bl	45.83	208.15	25,727	–15.69	3.97	0.07	0.20	0.885	0.007	0.097	0.008	3.49	0.77	
c	35.87	208.61	170	–14.17	2.71	–0.20	0.05	0.877	0.001	0.121	–0.002	2.81	0.19	Clementina
c	29.02	182.02	253	–13.65	3.36	0.28	0.02	0.868	0.002	0.102	–0.001	2.32	0.06	Lisa
c	48.41	191.44	312	–19.28	3.18	–0.12	0.03	0.811	0.004	0.197	0.009	1.78	0.19	Raymonde
c	32.65	208.66	398	–13.33	3.40	0.17	0.06	0.872	0.002	0.105	0.002	2.45	0.06	Yambika
c	40.86	199.46	442	–14.96	3.35	–0.21	0.02	0.866	0.001	0.124	0.000	2.16	0.12	Unitkak
c	30.68	187.28	694	–11.31	3.30	0.50	0.22	0.886	0.001	0.084	0.000	3.38	0.57	Akiko
c	37.23	207.86	703	–12.61	3.50	0.04	0.07	0.842	0.004	0.148	0.012	2.24	0.46	Olivia
c	34.92	205.81	737	–14.09	3.53	–0.43	0.04	0.876	0.004	0.108	0.005	2.06	0.43	Ugne
c	32.28	195.25	797	–13.78	2.08	0.01	0.07	0.884	0.001	0.101	0.001	2.34	0.16	
c	33.77	185.05	978	–14.23	3.73	–0.59	0.03	0.890	0.006	0.106	0.009	2.23	0.80	Uleken
c	44.14	201.58	2,741	–13.71	2.84	–0.47	0.17	0.877	0.004	0.111	0.011	2.73	0.73	Nadira
c	48.33	195.39	11,931	–12.87	3.56	–0.42	0.37	0.861	0.023	0.152	0.030	2.02	0.85	Yablochkina
cf	48.40	195.19	9,856	–20.52	2.62	–0.13	0.14	0.851	0.019	0.175	0.032	1.15	0.39	Yablochkina
co	49.07	202.62	34,147	–15.69	3.33	0.08	0.39	0.880	0.008	0.121	0.019	3.64	1.02	Cerridwen and Neyterkob
cof	32.46	205.08	3,733	–13.76	2.80	–0.10	0.21	0.896	0.009	0.090	0.008	2.81	1.15	Nimba Corona
cof	33.43	204.43	15,145	–13.76	2.80	–0.10	0.21	0.896	0.009	0.090	0.008	2.81	1.15	Nimba Corona
cof	48.06	204.44	39,511	–15.67	2.58	–0.21	0.23	0.873	0.009	0.130	0.015	2.78	0.70	
fe	40.85	209.96	264	–16.16	4.35	–0.27	0.22	0.884	0.008	0.100	0.000	3.45	0.57	
fe	42.80	195.45	287	–18.74	2.11	–0.04	0.04	0.845	0.002	0.155	–0.002	2.08	0.05	
fe	30.35	205.84	1,972	–15.39	2.30	0.21	0.15	0.883	0.003	0.091	0.001	3.09	0.32	
fe	42.41	195.94	2,561	–18.77	2.03	–0.34	0.04	0.842	0.009	0.189	0.014	1.85	0.21	
fe	36.60	209.62	4,128	–14.94	2.29	0.24	0.11	0.887	0.009	0.098	0.005	3.46	0.56	Kokyanwuti Mons (V–15)
fe	25.29	196.35	4,553	–12.86	2.08	1.04	0.20	0.910	0.008	0.073	0.005	3.16	0.78	
fe	38.54	206.57	6,761	–14.52	2.31	–0.36	0.17	0.862	0.011	0.123	0.004	2.99	0.54	
fe	28.37	199.19	14,246	–10.97	2.57	0.28	0.24	0.914	0.009	0.088	0.006	4.08	1.27	
fe	44.80	184.77	18,202	–17.10	2.93	–0.03	0.56	0.857	0.005	0.142	0.019	3.24	0.75	Nijole Mons
fe	32.40	206.97	18,361	–12.57	2.65	0.00	0.19	0.906	0.007	0.084	0.006	3.51	1.08	Garland Patera
fe	38.95	203.24	21,334	–15.57	2.57	–0.43	0.28	0.867	0.011	0.123	0.014	3.38	0.92	
fe	27.69	196.87	22,649	–11.66	2.51	0.28	0.45	0.909	0.008	0.081	0.008	4.30	1.52	
fe	30.12	207.07	26,152	–14.68	2.32	0.08	0.12	0.872	0.007	0.099	0.005	3.16	0.85	
fe	34.20	198.61	30,354	–14.66	2.35	–0.12	0.23	0.872	0.009	0.108	0.009	3.27	0.73	Dutrieu Patera
fe	26.04	197.23	30,661	–11.97	2.78	0.59	0.38	0.904	0.009	0.085	0.008	3.19	1.13	Ninisinna Mons
fe	40.13	194.00	44,093	–15.68	2.65	–0.14	0.28	0.878	0.012	0.110	0.014	2.83	0.54	Xtoh Mons
fe	39.18	207.10	58,585	–15.01	2.28	–0.46	0.20	0.868	0.011	0.121	0.010	2.83	0.72	Shala Mons
fe	40.36	206.75	64,329	–15.73	2.42	–0.50	0.20	0.866	0.011	0.119	0.010	2.29	0.48	Apakura Tholus

Table 2. Individual map unit properties and names for every geographically distinct example of each unit, arranged alphabetically by map symbol and then by increasing area. Each entry in the table corresponds to a single discrete example (for example, closed polygon) of the unit. The unit latitude and longitude provided for each table entry is the centroid location calculated within ArcGIS—continued.

Symbol	Lat (deg N)	Long (deg E)	Area (km^2)	Backscatter_Adj (dB)		Topography (km)[a]		Emissivity		Reflectivity		RMS Slope (deg)		IAU Name[1]
				Mean	1 Sigma	Mean	1 Sigma	Mean	1 Sigma	Mean	1 Sigma	Mean	1 Sigma	
fe	35.78	208.60	72,653	–14.96	2.54	–0.16	0.33	0.886	0.015	0.103	0.011	3.11	0.82	Kokyanwuti Mons (V–15)
fe	26.62	206.63	213,265	–14.84	2.61	0.18	0.19	0.881	0.015	0.096	0.013	1.94	0.62	Waka Mons, Asintmah Cor
pG	26.31	183.82	156,863	–12.08	2.72	0.62	0.25	0.892	0.012	0.084	0.007	3.77	1.01	Ganis Chasma
ph	44.41	193.57	14,811	–19.45	2.27	0.34	0.13	0.916	0.021	0.084	0.014	4.31	1.28	
pl	37.02	209.88	386	–14.94	2.29	0.24	0.11	0.887	0.009	0.098	0.005	3.46	0.56	
pl	37.22	209.23	625	–14.94	2.29	0.24	0.11	0.887	0.009	0.098	0.005	3.46	0.56	
pl	37.70	202.07	1,451	–17.17	2.72	0.26	0.14	0.844	0.006	0.136	0.007	3.19	0.79	
pl	45.18	196.76	1,898	–18.68	3.61	–0.05	0.21	0.865	0.006	0.129	0.036	1.71	0.32	
pl	35.27	190.33	2,007	–12.97	2.43	0.38	0.24	0.898	0.004	0.070	0.003	2.91	0.22	
pl	31.97	182.82	2,167	–15.98	3.01	–0.13	0.20	0.866	0.011	0.096	0.007	3.53	0.44	
pl	32.37	181.66	2,293	–14.02	2.60	–0.11	0.12	0.884	0.009	0.092	0.001	3.76	1.12	
pl	31.51	205.33	2,709	–13.04	2.51	–0.03	0.11	0.912	0.006	0.086	0.013	4.90	1.33	
pl	31.45	181.57	2,908	–14.10	2.55	0.33	0.15	0.890	0.007	0.091	0.009	5.10	1.03	
pl	37.15	198.37	3,654	–14.87	2.79	–0.05	0.05	0.876	0.007	0.112	0.004	2.46	0.28	
pl	33.58	208.88	3,864	–12.73	2.57	0.27	0.15	0.904	0.005	0.086	0.008	3.75	1.06	
pl	28.18	208.91	5,412	–12.76	2.84	0.32	0.12	0.896	0.011	0.081	0.003	2.57	0.78	
pl	35.84	207.22	5,482	–13.57	2.77	–0.28	0.19	0.889	0.008	0.104	0.007	3.70	0.81	
pl	44.96	191.66	7,870	–18.57	3.75	0.94	0.17	0.858	0.011	0.136	0.012	2.04	0.50	
pl	26.18	202.49	9,871	–13.99	2.48	0.29	0.19	0.880	0.011	0.083	0.002	3.03	0.52	
pl	27.32	203.92	11,524	–14.62	2.45	0.28	0.21	0.881	0.005	0.092	0.009	3.49	1.14	
pl	29.16	205.62	13,770	–14.76	2.37	0.37	0.18	0.879	0.008	0.101	0.011	3.83	1.36	
pl	37.84	201.05	45,063	–15.66	2.82	–0.05	0.20	0.863	0.015	0.116	0.010	2.72	0.56	
pl	37.66	184.77	66,916	–14.18	2.62	0.17	0.25	0.886	0.010	0.089	0.007	2.99	0.65	
pl	36.03	194.83	143,273	–13.66	2.66	0.04	0.23	0.899	0.012	0.080	0.006	3.21	0.82	
pLh	28.37	187.51	12,547	–12.21	2.74	–0.05	0.32	0.906	0.006	0.066	0.007	5.00	1.45	
pLl	28.64	188.04	1,222	–10.41	3.08	0.46	0.17	0.907	0.002	0.072	0.004	4.87	1.41	
pLl	27.76	191.15	3,600	–12.35	2.34	0.39	0.12	0.906	0.008	0.074	0.005	3.97	0.63	
pLl	30.97	187.73	4,754	–13.68	3.52	0.03	0.21	0.884	0.004	0.075	0.007	3.96	1.19	
pLl	32.05	190.46	11,601	–11.47	2.56	0.13	0.13	0.899	0.008	0.071	0.002	3.22	0.77	
pLl	27.55	187.52	16,066	–11.61	2.67	0.07	0.18	0.904	0.008	0.067	0.002	3.67	1.03	
pLl	29.73	188.34	21,251	–13.35	2.70	0.28	0.18	0.888	0.009	0.073	0.004	3.12	0.71	
pLl	26.25	190.71	87,476	–12.42	2.43	0.52	0.26	0.888	0.014	0.075	0.004	3.43	0.99	
pr_1	39.03	202.42	447	–16.65	1.87	–0.51	0.08	0.864	0.002	0.115	–0.001	2.98	0.45	
pr_1	25.28	195.71	572	–12.48	1.98	0.84	0.06	0.923	0.006	0.070	–0.001	2.99	0.67	
pr_1	25.25	195.19	699	–12.33	2.05	0.52	0.12	0.920	0.002	0.061	0.002	2.78	0.67	
pr_1	26.06	190.46	880	–14.13	2.02	0.49	0.07	0.880	0.005	0.072	0.001	2.48	0.19	
pr_1	40.01	180.21	1,066	–14.99	2.71	0.51	0.18	0.884	0.003	0.094	0.006	3.42	0.52	
pr_1	35.76	182.19	2,232	–15.47	2.35	–0.12	0.11	0.865	0.004	0.102	0.006	2.39	0.23	
pr_1	35.37	191.42	2,417	–12.79	2.13	0.18	0.15	0.898	0.005	0.076	0.001	2.83	0.52	
pr_1	26.99	187.11	4,650	–13.03	2.31	0.25	0.17	0.881	0.011	0.076	0.003	2.78	0.33	

Table 2. Individual map unit properties and names for every geographically distinct example of each unit, arranged alphabetically by map symbol and then by increasing area. Each entry in the table corresponds to a single discrete example (for example, closed polygon) of the unit. The unit latitude and longitude provided for each table entry is the centroid location calculated within ArcGIS—continued.

Symbol	Lat (deg N)	Long (deg E)	Area (km^2)	Backscatter_Adj (dB)		Topography (km)[a]		Emissivity		Reflectivity		RMS Slope (deg)		IAU Name[1]
				Mean	1 Sigma	Mean	1 Sigma	Mean	1 Sigma	Mean	1 Sigma	Mean	1 Sigma	
pr_1	34.42	208.72	5,641	–14.58	2.20	0.11	0.07	0.900	0.006	0.083	0.003	3.12	0.53	
pr_1	31.15	182.14	18,322	–16.48	2.38	0.16	0.26	0.872	0.008	0.091	0.005	3.14	0.82	
pr_1	25.67	180.80	22,407	–13.60	2.52	0.75	0.18	0.874	0.008	0.093	0.008	4.01	1.08	
pr_1	32.16	185.45	43,536	–15.55	2.72	–0.28	0.28	0.870	0.009	0.103	0.016	3.51	1.49	
pr_1	33.55	192.81	94,107	–12.66	2.28	–0.17	0.20	0.870	0.017	0.101	0.016	2.03	0.46	
pr_1	29.59	200.23	664,348	–13.55	2.69	0.24	0.37	0.894	0.013	0.084	0.009	3.17	1.16	
pr_2	28.40	194.21	217	–14.42	2.74	–0.96	0.05	0.911	0.004	0.075	0.000	2.09	0.09	
pr_2	28.28	192.22	316	–15.52	3.26	–0.01	0.08	0.885	0.005	0.078	–0.001	2.24	0.41	
pr_2	42.42	209.87	454	–18.58	2.74	–0.52	0.01	0.866	0.003	0.126	0.003	2.38	0.31	
pr_2	44.05	193.35	556	–23.33	2.01	0.29	0.02	0.941	0.003	0.053	0.001	3.28	0.48	
pr_2	28.78	193.55	569	–15.94	2.27	–0.37	0.18	0.913	0.003	0.080	0.000	2.38	0.94	
pr_2	29.34	195.97	634	–16.83	2.35	–0.71	0.12	0.892	0.006	0.098	0.009	2.02	0.38	
pr_2	43.68	204.32	671	–15.59	2.50	–0.28	0.11	0.862	0.002	0.136	0.010	4.23	0.84	
pr_2	25.88	185.89	1,256	–14.54	2.21	0.74	0.09	0.895	0.003	0.063	–0.003	3.00	0.15	
pr_2	35.43	195.53	1,413	–15.56	2.22	–0.05	0.06	0.891	0.002	0.083	0.001	1.97	0.34	
pr_2	41.77	208.91	2,106	–16.93	1.87	–0.37	0.11	0.868	0.003	0.114	0.001	2.08	0.22	
pr_2	43.94	201.37	3,093	–16.11	2.40	–0.36	0.18	0.870	0.004	0.129	0.011	2.83	0.60	
pr_2	29.03	209.50	3,268	–15.91	2.54	–0.12	0.06	0.876	0.011	0.116	0.013	1.77	0.37	
pr_2	42.40	205.29	3,269	–15.56	2.07	–0.87	0.06	0.886	0.006	0.115	0.006	1.90	0.38	
pr_2	46.78	201.99	4,812	–16.83	2.67	–0.29	0.35	0.858	0.003	0.148	0.018	3.02	0.88	
pr_2	36.49	195.28	5,485	–16.36	2.42	–0.36	0.07	0.898	0.009	0.092	0.005	2.02	0.35	
pr_2	43.49	195.74	6,843	–19.31	2.80	0.24	0.29	0.860	0.012	0.130	0.016	2.41	0.51	
pr_2	38.09	197.47	7,247	–17.76	2.01	–0.31	0.07	0.874	0.006	0.119	0.005	2.10	0.30	
pr_2	27.72	209.41	7,507	–16.40	2.62	0.08	0.09	0.880	0.009	0.111	0.018	1.12	0.27	
pr_2	33.83	208.14	12,930	–16.63	2.29	–0.03	0.07	0.893	0.007	0.097	0.006	2.06	0.31	
pr_2	41.78	202.52	20,259	–14.81	2.58	–0.71	0.27	0.866	0.006	0.125	0.011	2.36	0.72	
pr_2	28.30	204.21	37,308	–15.81	2.41	0.17	0.15	0.880	0.009	0.094	0.007	2.73	0.59	
pr_2	36.80	204.32	142,461	–18.16	3.22	–0.03	0.28	0.851	0.016	0.130	0.013	2.68	0.83	
pr_2	46.33	207.63	156,555	–16.59	2.30	–0.09	0.26	0.879	0.009	0.113	0.013	2.48	0.71	
pr_2	34.35	197.60	306,015	–16.34	2.71	–0.07	0.30	0.873	0.014	0.111	0.017	2.25	0.72	
pr_2	41.42	188.08	1,934,778	–18.26	3.25	–0.12	0.37	0.860	0.020	0.132	0.031	2.46	0.72	
pr_3	40.04	209.97	42	–15.99	4.79	–0.32	0.01	0.861	0.001	0.110	–0.005	2.80	–0.10	
pr_3	29.54	182.92	1,284	–15.27	2.34	0.09	0.10	0.885	0.010	0.083	0.006	3.72	0.93	
pr_3	40.22	209.22	3,468	–15.24	2.23	–0.39	0.04	0.865	0.005	0.126	0.003	3.14	0.29	
pr_3	49.72	181.07	4,218	–15.73	2.28	–0.95	0.06	0.839	0.001	0.159	0.004	2.52	0.23	
pr_3	39.75	204.54	4,953	–15.58	1.77	–0.53	0.12	0.875	0.007	0.110	0.009	2.54	0.31	
pr_3	49.46	183.75	6,522	–17.00	1.96	–0.75	0.06	0.840	0.003	0.166	0.003	2.45	0.21	
pr_3	30.68	180.63	7,636	–15.90	2.02	0.03	0.07	0.859	0.004	0.120	0.004	2.85	0.22	
pr_3	44.15	180.64	7,845	–15.98	2.05	–0.36	0.21	0.856	0.004	0.138	0.009	3.12	0.26	
pr_3	39.20	209.44	8,014	–14.13	2.16	–0.37	0.11	0.857	0.013	0.119	0.007	2.89	0.59	

Table 2. Individual map unit properties and names for every geographically distinct example of each unit, arranged alphabetically by map symbol and then by increasing area. Each entry in the table corresponds to a single discrete example (for example, closed polygon) of the unit. The unit latitude and longitude provided for each table entry is the centroid location calculated within ArcGIS—continued.

Symbol	Lat (deg N)	Long (deg E)	Area (km²)	Backscatter_Adj (dB)		Topography (km)[a]		Emissivity		Reflectivity		RMS Slope (deg)		IAU Name[1]
				Mean	1 Sigma	Mean	1 Sigma	Mean	1 Sigma	Mean	1 Sigma	Mean	1 Sigma	
pr_3	28.55	205.77	10,395	–14.19	1.98	0.17	0.12	0.870	0.008	0.098	0.004	2.74	0.51	
pr_3	36.55	207.38	32,282	–15.92	2.41	–0.09	0.15	0.856	0.011	0.134	0.014	2.43	0.51	
pr_3	42.66	202.14	525,006	–15.44	2.38	–0.49	0.21	0.863	0.012	0.128	0.016	2.65	0.54	
ps	29.80	191.92	1,110	–15.02	2.65	–0.71	0.42	0.906	0.008	0.079	0.006	3.26	0.72	
ps	29.75	191.00	1,136	–13.37	2.53	–0.81	0.32	0.888	0.004	0.083	0.014	5.12	1.30	
ps	30.02	192.30	3,979	–13.81	2.16	–0.49	0.18	0.888	0.010	0.086	0.003	1.95	0.54	
ps	30.08	209.72	5,041	–14.46	2.63	–0.01	0.24	0.896	0.005	0.101	0.009	2.88	0.38	
ps	46.02	187.70	5,140	–20.43	2.65	0.31	0.11	0.832	0.002	0.157	0.008	2.61	0.22	
ps	49.74	209.27	6,123	–14.09	2.46	–0.11	0.14	0.884	0.004	0.115	0.007	3.66	0.57	
ps	37.64	206.37	9,613	–17.45	3.18	–0.51	0.24	0.844	0.006	0.147	0.019	2.40	0.68	
ps	45.22	190.83	12,477	–17.30	3.62	0.69	0.22	0.862	0.023	0.122	0.023	2.82	1.08	
ps	38.68	180.42	12,620	–15.69	2.58	0.06	0.32	0.880	0.006	0.093	0.005	3.00	0.64	
ps	44.28	190.31	13,103	–18.74	2.91	0.47	0.30	0.867	0.016	0.121	0.019	2.75	0.66	
ps	49.51	204.36	16,398	–16.90	2.33	–0.57	0.17	0.887	0.008	0.116	0.011	2.23	0.58	
ps	49.48	201.47	19,412	–17.58	2.68	–0.45	0.25	0.878	0.007	0.125	0.008	2.71	0.53	
ps	39.80	189.33	23,539	–16.03	2.00	–0.01	0.16	0.867	0.016	0.115	0.015	2.49	0.46	
ps	39.98	183.15	32,664	–15.54	2.15	–0.11	0.20	0.874	0.010	0.113	0.008	3.05	0.70	
ps	44.92	195.74	83,797	–20.58	3.86	0.06	0.43	0.873	0.023	0.134	0.033	2.33	1.05	
ps	34.65	186.30	88,674	–14.89	2.59	–0.10	0.18	0.880	0.010	0.088	0.009	2.86	0.80	
ps	33.09	201.02	217,304	–15.20	2.78	0.18	0.39	0.873	0.016	0.105	0.013	2.93	0.93	
t	45.41	193.22	68	–16.75	4.45	0.81	0.09	0.881	0.002	0.099	–0.001	1.60	0.17	Nemesis Tessera
t	29.58	188.01	151	–12.57	2.91	0.51	0.04	0.891	0.002	0.061	–0.002	2.55	0.24	Lahevhev Tessera
t	28.33	202.09	169	–13.38	2.84	0.51	0.03	0.880	0.002	0.091	–0.002	2.10	0.07	
t	34.05	188.73	181	–11.75	2.75	0.03	0.04	0.888	0.002	0.061	–0.003	2.43	0.42	Lahevhev Tessera
t	40.62	181.15	209	–14.23	3.19	–0.16	0.03	0.877	0.002	0.123	0.001	2.40	0.36	Nemesis Tessera
t	27.69	191.69	223	–11.77	2.73	0.21	0.04	0.882	0.004	0.085	–0.004	3.44	0.31	Lahevhev Tessera
t	36.62	199.06	264	–13.09	3.17	–0.09	0.00	0.853	0.003	0.132	0.001	2.55	0.00	
t	27.04	187.69	272	–10.40	2.68	0.22	0.10	0.893	0.005	0.074	–0.002	3.91	0.25	Lahevhev Tessera
t	36.29	199.99	307	–13.05	3.35	–0.17	0.02	0.860	0.004	0.120	–0.001	2.68	0.25	
t	27.99	202.39	341	–13.46	2.85	0.29	0.04	0.881	0.002	0.087	–0.002	2.71	0.16	
t	41.46	189.64	373	–14.40	3.44	0.41	0.02	0.855	0.003	0.133	0.001	2.43	0.11	Nemesis Tessera
t	34.81	184.05	388	–13.63	3.05	–0.09	0.05	0.882	0.002	0.101	–0.003	3.25	0.42	Athena Tessera
t	34.99	181.54	413	–13.90	3.48	–0.25	0.02	0.875	0.003	0.107	–0.001	1.82	0.09	Athena Tessera
t	29.65	188.52	433	–12.02	3.10	–0.01	0.11	0.879	0.006	0.072	–0.003	3.68	0.26	Lahevhev Tessera
t	36.72	198.15	453	–12.70	3.19	–0.15	0.03	0.879	0.005	0.106	0.001	1.94	0.08	
t	45.39	193.44	457	–17.82	4.13	0.76	0.11	0.898	0.011	0.103	0.011	1.84	0.46	Nemesis Tessera
t	33.65	191.48	458	–11.57	2.92	–0.21	0.03	0.884	0.001	0.085	0.003	2.16	0.18	Lahevhev Tessera
t	34.98	182.07	462	–14.13	3.27	–0.26	0.03	0.876	0.005	0.119	–0.002	1.89	0.14	Athena Tessera
t	29.45	188.33	494	–12.78	3.12	0.35	0.12	0.883	0.003	0.068	0.002	3.39	0.24	Lahevhev Tessera
t	27.91	202.01	536	–12.78	2.77	0.45	0.06	0.891	0.003	0.095	0.012	3.38	1.03	

Table 2. Individual map unit properties and names for every geographically distinct example of each unit, arranged alphabetically by map symbol and then by increasing area. Each entry in the table corresponds to a single discrete example (for example, closed polygon) of the unit. The unit latitude and longitude provided for each table entry is the centroid location calculated within ArcGIS—continued.

Symbol	Lat (deg N)	Long (deg E)	Area (km^2)	Backscatter_Adj (dB)		Topography (km)[a]		Emissivity		Reflectivity		RMS Slope (deg)		IAU Name[1]
				Mean	1 Sigma	Mean	1 Sigma	Mean	1 Sigma	Mean	1 Sigma	Mean	1 Sigma	
t	36.80	200.83	574	–12.22	3.06	–0.27	0.17	0.883	0.005	0.106	0.005	3.52	0.51	
t	30.43	186.48	623	–14.50	3.29	0.30	0.08	0.898	0.004	0.080	0.002	3.11	0.65	Lahevhev Tessera
t	27.10	188.24	816	–9.95	2.62	–0.05	0.08	0.895	0.006	0.077	–0.002	4.43	0.69	Lahevhev Tessera
t	27.69	187.52	897	–10.08	2.59	–0.06	0.41	0.910	0.003	0.070	0.000	4.87	1.20	Lahevhev Tessera
t	25.11	200.42	920	–12.50	3.04	0.30	0.07	0.887	0.008	0.069	0.000	3.14	0.36	Lahevhev Tessera?
t	34.24	189.18	1,082	–12.74	2.89	–0.23	0.08	0.885	0.003	0.078	0.002	1.74	0.16	Lahevhev Tessera
t	37.79	190.02	1,188	–12.43	2.84	0.09	0.10	0.874	0.007	0.086	0.003	2.84	0.41	
t	28.02	188.58	1,394	–10.80	2.68	0.20	0.26	0.915	0.002	0.070	0.003	5.57	1.27	Lahevhev Tessera
t	36.09	182.31	1,461	–13.29	2.78	–0.13	0.07	0.877	0.005	0.106	0.004	3.24	0.41	Athena Tessera
t	30.16	182.22	1,588	–14.39	2.83	0.36	0.29	0.883	0.009	0.096	0.010	6.90	1.90	Athena Tessera
t	26.01	191.89	1,806	–10.73	2.63	0.97	0.14	0.915	0.006	0.077	0.009	4.72	1.23	Lahevhev Tessera
t	37.05	209.48	1,841	–13.09	2.81	0.25	0.09	0.901	0.006	0.100	0.010	4.69	1.40	
t	27.65	188.24	1,935	–10.58	2.66	–0.01	0.19	0.916	0.004	0.066	0.003	5.91	1.18	Lahevhev Tessera
t	35.85	180.30	3,189	–14.27	3.39	–0.19	0.07	0.883	0.011	0.103	0.005	2.79	1.05	Athena Tessera
t	25.81	199.06	3,679	–10.60	2.84	0.37	0.09	0.918	0.009	0.083	0.005	4.47	1.35	Lahevhev Tessera
t	47.31	181.14	3,736	–14.81	3.25	–0.57	0.12	0.862	0.009	0.131	0.006	2.64	0.73	
t	29.14	182.81	4,684	–14.25	3.20	0.51	0.25	0.887	0.006	0.082	0.012	4.04	0.95	Athena Tessera
t	35.97	184.91	4,930	–12.31	2.79	–0.05	0.24	0.896	0.008	0.085	0.009	4.13	1.05	Athena Tessera
t	34.89	180.98	5,250	–13.32	3.16	–0.35	0.31	0.890	0.012	0.099	0.010	4.00	2.35	Athena Tessera
t	47.57	187.61	5,847	–17.95	4.12	0.09	0.13	0.827	0.008	0.157	0.023	2.35	0.73	
t	33.91	192.47	6,121	–12.37	3.06	0.25	0.27	0.892	0.010	0.085	0.003	3.02	0.56	Lahevhev Tessera
t	28.18	186.31	6,250	–12.18	2.79	0.07	0.35	0.910	0.006	0.075	0.004	4.41	1.12	Lahevhev Tessera
t	28.72	188.96	6,756	–11.37	3.04	0.30	0.16	0.897	0.006	0.075	0.004	3.80	0.99	Lahevhev Tessera
t	28.97	187.31	7,798	–11.26	2.97	0.42	0.30	0.901	0.006	0.074	0.008	4.93	1.69	Lahevhev Tessera
t	27.33	190.73	8,696	–11.04	2.76	0.51	0.19	0.906	0.009	0.075	0.006	4.65	1.58	Lahevhev Tessera
t	32.15	187.13	11,585	–13.44	3.05	–0.12	0.14	0.888	0.009	0.082	0.006	3.43	1.04	Lahevhev Tessera
t	27.77	201.31	11,828	–11.38	2.92	0.71	0.24	0.905	0.012	0.084	0.011	4.28	1.78	
t	34.43	182.92	11,963	–13.26	3.05	–0.22	0.20	0.892	0.012	0.090	0.011	3.91	1.85	Athena Tessera
t	34.88	191.00	12,930	–11.70	2.74	0.23	0.29	0.897	0.009	0.071	0.003	3.44	0.93	Lahevhev Tessera
t	40.01	181.19	16,066	–13.68	2.98	0.35	0.25	0.887	0.009	0.088	0.006	3.69	0.85	Nemesis Tessera
t	30.18	187.42	17,285	–12.30	3.38	0.36	0.22	0.891	0.008	0.086	0.009	4.24	1.78	Lahevhev Tessera
t	46.15	194.14	18,024	–15.77	3.85	0.81	0.56	0.878	0.012	0.094	0.016	3.13	1.09	Nemesis Tessera
t	40.91	186.26	24,088	–13.13	3.25	0.54	0.30	0.889	0.015	0.092	0.009	3.77	1.16	Nemesis Tessera
t	32.44	180.71	28,374	–12.32	3.24	0.20	0.24	0.914	0.012	0.081	0.012	4.95	1.90	Athena Tessera
t	31.63	189.17	60,484	–11.32	2.93	0.41	0.31	0.906	0.011	0.071	0.004	4.29	1.55	Lahevhev Tessera
t	26.58	194.08	88,881	–11.37	2.92	0.86	0.23	0.928	0.012	0.071	0.005	4.01	1.40	Lahevhev Tessera

[1]Izumi Patera and Razia Patera preserve no unique material units, and hence are not listed here